THESIS FOR THE DEGREE OF DOCTOR OF PHILOSOPHY

Novel Functionalized Nanopores for Plasmonic Sensing

Bita Malekian

Department of Chemistry and Chemical Engineering

Division of Applied Chemistry

Chalmers University of Technology

Gothenburg, Sweden 2021

Novel Functionalized Nanopores for Plasmonic Sensing

BITA MALEKIAN

ISBN 978-91-7905-538-7

Doktorsavhandlingar vid Chalmers tekniska högskola

Ny serie nr 5005

ISSN 0346-718X

Department of Chemistry and Chemical Engineering

Chalmers University of Technology

SE-412 96 Gothenburg

Sweden

Telephone: +46 (0) 31-772 1000

Cover:
Cross-section FIB-SEM (focused ion beam scanning electron microscopy) images of plasmonic nanowells and nanocaves and cross-section SEM image of plasmonic nanopores with double gold films, together with schematics that illustrate material-specific functionalization and protein binding inside the cavities. The graph shows resonance shift upon protein binding inside the nanowells and nanocaves.

Printed by Chalmers Reproservice
Gothenburg, Sweden 2021

Novel Functionalized Nanopores for Plasmonic Sensing

Bita Malekian
Department of Chemistry and Chemical Engineering
Chalmers University of Technology

Abstract

Nanoplasmonic sensors offer a label-free platform for real-time monitoring of biomolecular interactions by tracking changes in refractive index through optical spectroscopy. However, other surface sensitive techniques such as conventional surface plasmon resonance offer similar capabilities with equal or even better resolution in terms of surface coverage. Still, plasmonic nanosensors provide unique possibilities when the nanoscale geometry itself is of interest. By taking the advantage of nanofabrication technology, it is possible to engineer nanostructures with controllable dimensions, curvature and optical properties to study nanometer-sized biomolecules, such as proteins.

This thesis presents different types of nanoplasmonic sensing platforms, each with a unique geometry in which biomolecules can be probed through plasmonic read out. Two of the structures were fabricated by short-range ordered colloidal self-assembly and etching of the solid support underneath a nanohole array. The structures are denoted as ‘nanocaves’ and ‘nanowells’ depending on the degree of anisotropy. By suitable surface functionalization, the geometry of the plasmonic nanocavities was utilized for location-specific detection of proteins. In addition, nanowells were employed to investigate curvature-dependent biomolecular interactions.

We have also developed subwavelength apertures in optically thin silicon nitride membranes covered with continuous metal films, referred to as solid-state ‘nanopores’. Plasmonic nanopores in suspended metal-insulator-metal films were fabricated in short-range ordered and long-range ordered arrays using short-range ordered colloidal self-assembly and electron beam lithography, respectively. Both methods prevent the metal from ending up on the silicon nitride walls which is of paramount importance for plasmonic properties and selective chemical functionalization. Preparing nanopores with identical structure but different aperture ordering provides the opportunity to understand how aperture ordering influences plasmonic response, particularly with respect to the nature of far field spectral features. Long-range ordered vs. short-range ordered nanopores exhibit similar optical properties with only a few differences in the plasmonic response.

By appropriate material-specific modification (thiol and trietoxysilane chemistry) plasmonic nanopores were employed for detection of average sized proteins (~ 60 kg/mol) inside the pores. In addition to nanoplasmonic sensing, we could also construct a credible mimic (in terms of geometry) of nuclear pore complexes, when the size of the solid state nanopores approaches ~ 50 nm. The unique geometry and size of nanopores (diameter ~ 50 nm) opens up the possibility to mimic the geometry of biological nanomachines with integrated optical sensing capabilities.

Keywords: plasmonic nanostructures, nanopores, nanoplasmonic sensor, nanowells, nanocaves, surface plasmon resonance, colloidal lithography, electron beam lithography, proteins, nuclear pore complex, extinction spectra, label-free sensing

LIST OF PUBLICATIONS

This thesis is based on the following appended papers:

I, Fabrication and Characterization of Plasmonic Nanopores with Cavities in the Solid Support

Bita Malekian, Kunli Xiong, Gustav Emilsson, Jenny Andersson, Cecilia Fager, Eva Olsson, Elin Larsson-Langhammer, and Andreas Dahlin. "Fabrication and characterization of plasmonic nanopores with cavities in the solid support." *Sensors* 17, no. 6 (2017): 1444.

II, Detecting Selective Protein Binding Inside Plasmonic Nanopores: Toward a Mimic of the Nuclear Pore Complex

Bita Malekian, Rafael Schoch, Timothy Robson, Gustav Ferrand-Drake del Castillo, Kunli Xiong, Gustav Emilsson, Larisa Kapinos, Roderick YH Lim, and Andreas Dahlin. "Detecting Selective Protein Binding inside Plasmonic Nanopores: Towards a Mimic of the Nuclear Pore Complex." *Frontiers in chemistry* 6 (2018): 637.

III, Nanoplasmonic Sensing Architectures for Decoding Membrane Curvature-Dependent Biomacromolecular Interactions

Ferhan Abdul Rahim, Joshua A. Jackman, Bita Malekian, Kunli Xiong, Gustav Emilsson, Soohyun Park, Andreas B. Dahlin, and Nam-Joon Cho. "Nanoplasmonic sensing architectures for decoding membrane curvature-dependent biomacromolecular interactions." *Analytical chemistry* 90, no. 12 (2018): 7458-7466.

IV, Nanoplasmonic Sensor Detects Preferential Binding of IRSp53 to Negative Membrane Curvature

Gustav Emilsson, Evelyn Röder, Bita Malekian, Kunli Xiong, John Manzi, Feng-Ching Tsai, Nam-Joon Cho, Marta Bally, and Andreas Dahlin. "Nanoplasmonic sensor detects preferential binding of IRSp53 to negative membrane curvature." *Frontiers in chemistry 7 (2019): 1.*

V, Optical Properties of Plasmonic Nanopore Arrays Prepared by Electron Beam and Colloidal Lithography

Bita Malekian, Kunli Xiong, Evan S. H. Kang, John Andersson, Gustav Emilsson, Marcus Rommel, Takumi Sannomiya, Magnus P. Jonsson and Andreas Dahlin. "Optical properties of plasmonic nanopore arrays prepared by electron and colloidal lithography." *Nanoscale Advances 1, no. 11 (2019): 4282-4289*

CONTRIBUTION REPORT

Paper I
Development, fabrication and scanning electron microscopy characterization of plasmonic nanowells and nanocaves with guidance of K.X. Optical characterization of the plasmonic nanostructures. Contributed to the writing of the manuscript.

Paper II
Fabrication and characterization of plasmonic nanopores. Performed refractometric sensing experiments of avidin and biotin-BSA binding to functionalized nanopores. Contributed to the writing of the manuscript.

Paper III
Fabrication and characterization of plasmonic nanowells.

Paper IV
Fabrication and characterization of plasmonic nanowells.

Paper V
Performed all experimental work including development of plasmonic nanopores with electron beam lithography approach. Development of plasmonic nanopores with CL method in collaboration with K.X. Comparing the optical properties of the nanopores prepared by EBL and CL methods experimentally. Contributed to the writing of the manuscript.

PAPERS NOT INCLUDED

The following papers are excluded from the thesis:

A: Gating Protein Transport in Solid Sate Nanopores by Single Molecule Recognition

Emilsson Gustav, Yusuke Sakiyama, Bita Malekian, Kunli Xiong, Zeynep Adali-Kaya, Roderick YH Lim, and Andreas B. Dahlin. "Gating protein transport in solid state nanopores by single molecule recognition." *ACS central science* 4, no. 8 (2018): 1007-1014.

B: Polymer Brushes in Solid-State Nanopores Form an Entropic Impenetrable Barrier for Proteins

Emilsson, Gustav, Kunli Xiong, Yusuke Sakiyama, Bita Malekian, Viktor Ahlberg Gagnér, Rafael L. Schoch, Roderick YH Lim, and Andreas B. Dahlin. "Polymer brushes in solid-state nanopores form an impenetrable entropic barrier for proteins." *Nanoscale* 10, no. 10 (2018): 4663-4669.

Acronyms

AFM	Atomic force microscopy
ACH	Aluminum chlorohydrate
AC	Alternating current
AH	Alpha-helical
APTES	(3-aminopropyl)triethoxysilane
ATR	Attenuated total internal reflection
BSA	Bovine serum albumin
CL	Colloidal lithography
Da	Dalton
DEP	Dielectrophoresis
EBL	Electron beam lithography
FDTD	Finite-difference time-domain
FG	Phenylalanine-glycine
FIB-SEM	Focused ion beam scanning electron microscopy
KOH	Potassium hydroxide
LPCVD	Low pressure chemical vapor deposition
LOD	Limit of detection
LSPR	Localized surface plasmon resonance
MIM	Metal-insulator-metal
NPC	Nuclear pore complex
PVD	Physical vapor deposition
PECVD	Plasma-enhanced chemical vapor deposition
PBS	Phosphate buffered saline
PEG	poly(ethylene glycol)

QCM-D	Quartz crystal microbalance with dissipation monitoring
RSA	Random sequential adsorption
RDF	Radial distribution function
RI	Refractive index
RIE	Reactive ion etching
SEM	Scanning electron microscopy
Si	Silicon
SPR	Surface plasmon resonance
SP	Surface plasmon
SPP	Surface plasmon polariton
SLB	Supported lipid bilayer
TIR	Total internal reflection
TEM	Transmission electron microscopy
UV	Ultraviolet

Contents

1

Introduction

Nanostructures can be engineered to exhibit unique physical and optical properties that are not present in their corresponding bulk counterparts [1]. The enormous progress of nanotechnology over the past few decades has made it possible to engineer nanostructure platforms compatible in size and geometry for studying nanometer-sized biomolecules [2]. Protein molecules for instance with typical diameter of ~ 5 nanometer govern most of the human body functions and hence, studying their function is of great importance to deeply understand how life works at the molecular level [3, 4]. However, in-depth understanding of the function of nanometer-sized biomolecules such as proteins, particularly at their native state, is challenging and preferably requires a label-free platform. Among various types of engineered nanostructures, plasmonic nanostructures have gained special attention as they offer the possibility to study biomolecules in a label-free manner (i.e. removing the need for fluorescence labeling) [5, 6]. When nanostructures are engineered properly, light can couple to nanoscale apertures in a metal film, exciting so-called surface plasmons. Surface plasmons are sensitive to changes in the refractive index of their nanoenvironment and therefore, can be used as probes for label-free monitoring of molecular interactions [7, 8].

Nanoplasmonic sensors have emerged over the last decades and took much attention not only due to their capability to create strongly localized electromagnetic field enhancements but also due to the unique possibilities they offer compared to conventional surface plasmon resonance (SPR) instruments [6, 9]. Nanoplasmonic sensors are usually referred to plasmonic sensors based on nanostructures, mainly nanoparticles and nanohole arrays. The detection principle of nanoplasmonic sensing is similar to conventional SPR where the refractive index increases upon binding of molecules to the sensor surface [7]. The increase in the refractive index induces a redshift in the plasmon resonance which is detectable by some form of optical spectroscopy [8]. The plasmons excited in plasmonic nanostructures are typically associated with a shorter probing

length (tens of nm) compared to conventional SPR (a few hundred nm from a metal surface) [2]**.** The shorter penetration depth of surface plasmons evanescent field can reduce the risk of false positive reading, so-called bulk effect, which is considered as an advantage of plasmonic nanostructures over the conventional SPR [2]. Nevertheless, as long as resolution in terms of surface coverage is the most relevant parameter of sensor performance in most situations, it is hard for nanoplasmonic sensors to compete with the conventional SPR as plasmonic nanostructures and the conventional SPR have, at best, similar performance in resolution [4]. In addition, quantification of the amount of bound analyte is also challenging compared to conventional SPR, as the planar SPR permits the variation in only one spatial dimension [10]. Moreover, surface modification is more complex in plasmonic nanostructures as several materials tend to be exposed, again in contrast to SPR [11]. This suggests limited use of nanoplasmonic sensors to investigate biomolecular interactions, at least through ordinary refractometric sensing. Still, if one can utilize the nanostructure itself (such as its curvature) to address nanoscale geometry-related questions, the sensors offer unique possibilities not achievable by planar SPR. For instance, various types of plasmonic nanostructures were used for studying biomolecular processes on curved lipid membranes [12] and the capability of polymer brushes to form barriers toward proteins transport [13]. Having several materials in the nanostructure might also turn into an advantage as it offers the possibility to direct molecular binding to specific regions/materials of the nanostructure using suitable surface functionalization.

Besides the afore mentioned capabilities of the nanoplasmonic sensors, the use of nanoscale geometry may provide other interesting benefits. Plasmonic nanoparticles for instance, as an extremely miniaturized sensors, offer the possibility of resolving individual binding events [14, 15]. However, it does not address questions regarding the influence of negative curvature on molecular interactions or mimicking biological nanopores. Solid-state nanoholes instead, have been particularly useful for this purpose by creating regions with negative curvature. Nanoholes-based biosensing was first reported by Brolo *et al*. which has shown the refractometric detection of protein adsorption [16]. In parallel, plasmonic nanohole arrays on solid supports were developed by Dahlin *et al*. and used for studying the protein-membrane interactions in real-time in 2005 [17]. In addition to refractometric detection, the optical near-fields enhancement in plasmonic nanostructures were exploited in other optical methods such as surface enhanced Raman scattering and plasmon-enhanced fluorescence spectroscopy [18-24]. Nanopores/nanoholes in continuous

metal films with plasmonic functionality also offers the opportunity for implementing electrochemistry, dielectrophoresis or temperature control [25-27]. Solid-state nanoscale apertures in thin membranes, in particular, gained much attention mainly due to their capability of label-free single-molecule investigation of biomolecules such as DNA [28].

The work presented herein is aimed towards introducing novel plasmonic nanostructures, each with unique geometry for different applications. I discuss different nanofabrication approaches and their challenges for developing plasmonic nanoscale cavities and pores in solid supports. I have developed plasmonic 'nanopores' in suspended metal-insulator-metal films with excellent structure control using two different approaches. In one approach, short-range ordered colloidal self-assembly was used as a high throughput method to pattern nanopore arrays on freestanding silicon nitride (SiN_x) membranes. In the other approach, I used electron beam lithography (EBL) to pattern long-range ordered nanopore arrays on optically thin SiN_x membranes in a well-controlled and highly reproducible manner. EBL offers not only high resolution and arbitrary patterns but also increases the robustness or the yield of fabrication in terms of the number of intact membranes. The precise fabrication methods presented here provide the possibility to elucidate how aperture ordering (long-range vs. short-range) of identical structures influences their optical response. Moreover, both methods prevent the metal from ending up on to the nanopore walls in the SiN_x membrane which is of paramount importance for plasmonic functionality and for selective surface functionalization.

Further, two other types of nanostructures were fabricated by short-range ordered colloidal self-assembly and etching the solid support underneath a nanohole array. The created cavities in the solid support are denoted as 'nanocaves' and 'nanowells' depending on the degree of anisotropy (wet etching or dry etching). I describe how the geometry of nanocaves and nanowells influence their optical properties and refractometric sensitivity, and how this can be utilized for location-specific sensing. By suitable surface functionalization, plasmonic nanowells were also utilized for studying curvature-dependent biomolecular interactions.

I have developed label-free nanoplasmonic sensing platforms with optical real-time readouts to provide insight into complex biophysical phenomena. The unique geometry of the nanoscale cavities and SiN_x membrane nanopores made it possible to perform location-specific protein binding using suitable surface functionalization. In addition, when the size of SiN_x nanopores

approaches ~ 50 nm, we could construct a credible mimic of the geometry of nuclear pore complexes [29-32].

2

Plasmonics

2.1 Surface Plasmon Resonance

Surface plasmons, for the first time, were observed in the spectrum of light diffracted on a metallic diffraction grating as 'anomalies' by Wood in 1902 [33] . Fano demonstrated that these anomalies are related with the excitation of electromagnetic surface waves on the surface of the diffraction grating [7, 34]. Later in 1968, Otto explained that the strong decrease in the reflection in the attenuated total reflection method is due to the excitation of surface plasmons [35, 36].

Surface plasmons (SPs) are propagating electromagnetic waves at the metal-dielectric interface, evanescently confined to the interface [4]. Surface plasmon polaritons (SPPs) are the resonant surface plasmons which is the result of electromagnetic fields (light) coupling to the oscillations of the conduction electrons in the metal [37]. The coupling of the incident photon to the surface plasmons occurs if both the energy (frequency) and momentum of the incoming photon are matched with surface plasmons. However, there is a momentum mismatch between a free-space photon and surface plasmons as they have different dispersion relations.

Dispersion relation is a mathematical function describing the relation between the momentum and frequency. The dispersive properties of a metal can be described through a complex dielectric function of $\epsilon(\omega)$, $\epsilon(\omega) = \mathrm{Re}\,\epsilon(\omega) + \mathrm{Im}\,\epsilon(\omega)$. For a single interface between two semi-infinite materials, a metal and a dielectric, Maxwell' equations yield:

$$\frac{k_{zm}}{\epsilon_{zm}} = -\frac{k_{zd}}{\epsilon_d} \tag{1}$$

and:

$$\epsilon_i \left(\frac{\omega}{c}\right)^2 = {k_x}^2 + {k_{zi}}^2 \tag{2}$$

Where k_x denotes the *x* component of the SPP wavevector in parallel to the interface and in the direction of propagation. k_{zi} denotes the *z* component of the SPP wavevector in both metal and dielectric (medium *i*), perpendicular to the interface. Combining the two expressions above gives the dispersion relation for a SPP propagating at the interface of a metal-dielectric:

$$k_x(\omega) = \frac{\omega}{c}\sqrt{\frac{\epsilon(\omega)\epsilon_d}{\epsilon(\omega)+\epsilon_d}} \qquad (3)$$

Assuming a typical metal and dielectric with a negative Re $\epsilon\ (\omega)$ and | Re $\epsilon\ (\omega)| > \epsilon_d$, the SPP wavevector k_x is always larger than the incident photon wavevector in air or vacuum. Therefore, a coupling mechanism is required to increase the photon momentum (the *x* component of the wavevector) to excite the surface plasmons. There are two common ways to provide the extra momentum needed to excite SPs: Grating coupling mechanism and total internal reflection (TIR) Kretschmann configuration. Here we describe both configurations even though we have only used the grating coupling mechanism to excite SPs in our nanostructured surfaces.

2.2 Grating Coupling Mechanism

As explained in the previous section a photon traveling in medium *i* does not couple to the SPs as photon always has a smaller wave vector than that of SPs under normal circumstances. Creating periodic structures on the metal surface can add the missing momentum to the photon wave vector. In principle, any shape irregularities with a period of Λ in the metal surface can increase the photon wave vector by multiplies of $2\pi/\Lambda$ which can add the missing momentum to the photon wave vector [4]. The grating resonance condition for the SPs excitation can be written as:

$$\mathrm{Re}(k_x) = k\sin(\Theta) \pm j\frac{2\pi}{\Lambda} \qquad (4)$$

Where Θ is the angle of the incident photon wave vector, against the surface normal, *k* is the photon wave vector and *j* is a positive integer indicating the diffraction order of the grating. **Figure 1** shows a schematic of the grating coupling mechanism. For the SPs excitation, periodicity 'Λ' should match the SPPs wavelength. Therefore, a periodic structure in a metallic surface enables

coupling of light to the SPs at the metal-dielectric interface by the grating coupling mechanism. Such a structure could be a thin metal film containing arrays of holes with a certain periodicity.

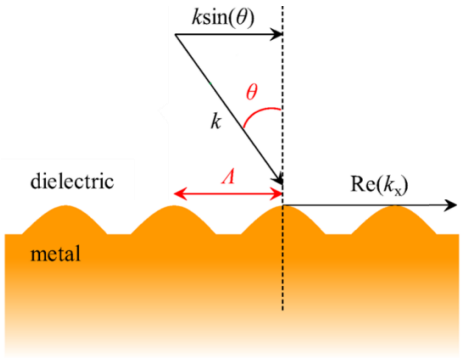

Figure 1. Schematic of grating coupling mechanism. The photon wavevector along the metal dielectric interface increases due to diffracted waves, when interacting with a periodic grating (Figure from [4]).

2.3 Prism Coupling Mechanism

One approach to solve the momentum mismatch between the wavevector of light and the surface plasmon is using prism coupling, utilizing a high refractive index prism and the attenuated total internal reflection (ATR) method [7]. Kretschmann configuration and Otto configuration are the most common methods in prism coupling to excite SPs [38]. In this section, Kretschmann configuration is described as one of the most frequently used method in conventional SPR to excite SPs using prism coupling mechanism.

In the Kretschmann TIR configuration, a light wave passing through a high refractive index prism (compared to the dielectric in contact with the metal), undergoes total internal reflection at the base of the prism, above a certain critical angle according to Snell's law, producing an evanescent wave penetrating a relatively thin metal film. The evanescent wave, propagating at the metal-dielectric interface, can couple to the SP by controlling the angle of the incidence. **Figure 2** illustrates the schematic of the prism coupling mechanism using Kretschmann configuration. The resonance condition for matching the photon momentum with the SP in the Kretschmann TIR configuration is:

$$Re(k_x) = n_p k_0 \ sin(\theta) \tag{5}$$

Where Θ denotes the angle of the incidence, k_0 is the photon wave vector, n_p is the refractive index of the prism and, k_0 is the x component of the SPP wavevector. Thus, if this resonance condition is fulfilled, surface plasmons can be excited through prism coupling mechanism.

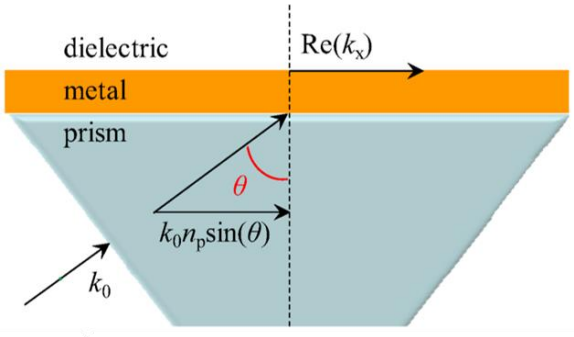

Figure 2. Schematic of prism coupling mechanism in Kretschmann TIR configuration. The incident light gains extra momentum when traveling through the higher refractive index medium, prism, compared to the dielectric medium (Figure from [4]).

2.4 Commercialized/Conventional SPR

Conventional SPR (planar SPR) sensors are planar thin gold film refractometers that measure changes in the refractive index at the metal surface, typically employing Kretschmann TIR configuration. When the resonance condition is satisfied, the incident light couples to the surface plasmons. In the Kretschmann TIR configuration, the SPP excitation manifests itself as a minimum in the angular spectrum of the reflected light [39]. Since the light-SP coupling condition is altered by changes in the refractive index, there will be a shift in the minimum/dip of the reflection upon changes in the refractive index. The dip of the reflection is shifted towards higher angles upon increasing in the refractive index of the close proximity to the metal surface, or towards the lower angles when the refractive index is decreased [40]. Monitoring the shift in the dip of the angular spectrum of the reflected light due to changes in the refractive index is typically the basis of commercial/planar SPR instruments.

Limit of Detection (LOD), also called resolution, is probably the most relevant factor in sensor performance, among other performance characteristics of the SPR such as sensitivity,

reproducibility and accuracy [40]. LOD is sometimes defined in terms of number of bound molecules such as in extremely miniaturized sensors [41-43]. However, an alternative way to define LOD is based on surface coverage (mass per unit area) [4, 44]. Surface coverage is related to the concentration (C) of the analyte in solution through the dissociation constant (K_D) of the receptor according to the simplest Langmuir binding equilibrium model:

$$\frac{\Gamma}{\Gamma_{max}} = \frac{c}{c + k_D} \tag{6}$$

Where Γ and Γ_{max} are the surface coverage and the maximum surface coverage, respectively. The ratio Γ/Γ_{max} indicates the probability of a receptor on the sensor surface to have a target bound analyte, implying that the analyte needs to diffuse to the sensor surface first in order to bind to the receptor. In many real-world sensor applications, there are plenty of molecules available and most biomolecular interactions are reversible, so it is more relevant to define LOD in terms of surface coverage rather than the number of molecules in order to include the analyte concentration and also the reversible nature of most biomolecular interactions. Much literature indicates that nanoplasmonic sensors have similar performance in resolution, at best, to planar/conventional SPR for detecting analytes [6]. Nevertheless, nanoplasmonic sensors offer unique opportunities not possible to achieve by conventional SPR [45].

3

Plasmonic Nanopore Arrays in Suspended Metal-Insulator-Metal Films

Solid-state nanopores, nanometer-sized apertures in thin membranes, are of great interest in nanotechnology due to their promising applications in studying biomolecules and their robustness, versatility and ease of integration in CMOS processing [46-48]. To date, much effort has been directed towards controlled fabrication of individual nanopores for single molecule experiments such as DNA sequencing using ion current measurements [49, 50]. However, relatively little work has been spent on development of 'arrays of nanopores' which enables novel applications not possible to achieve by single nanopores. For instance, a single nanopore is not capable of being used for efficient filtration, whereas arrays of nanopores in thin membranes are utilized as biomolecular filtration with high diffusive flux [51-53]. Further, arrays of nanoscale apertures in thin metal films, under certain condition, enables the excitation of surface plasmons which provides refractometric detection/sensing [54].

However, there are several challenges for a controlled and reliable fabrication of nanopore arrays in continuous metal films which have not been addressed yet. The techniques which are utilized for the fabrication of single nanopores, such as focused ion beam (FIB)-drilled nanopores, is not feasible to upscale for fabrication of arrays. One approach for patterning could be photolithography, but the feature size attainable with this technique is limited to at least hundreds of nanometers [55]. Electron beam lithography (EBL) offers high resolution but has mainly been employed to fabricate nanopores using positive-tone resist [56]. The drawback with using positive resist, when metal film deposition is part of the fabrication process, is that the metal ends up on the existing nanopore sidewalls in the dielectric membrane since the directionality is never perfect, which in turn disturbs plasmonic properties and also complicates the subsequent selective surface functionalization of the pore interior [57, 58].

To overcome these challenges, one approach is using CL to create nanopores in short-range as well as hexagonal long-range ordered patterns [59-64]. However, arbitrary patterns (tuning periodicity for a long-range ordered pattern) are not feasible with CL and the fabrication process requires high stability for the dielectric membranes to remain intact during lift-off [65]. To tackle the latter, we have developed a CL method which eliminates the risk of breaking membranes during the lift-off. In another approach, I have employed EBL with using negative resist to construct plasmonic nanopore arrays in dielectric membranes with metal-free pore interiors in the membrane [66]. By using negative resist, the metallic apertures are formed before the etch step that transfers the pores to the membrane, preventing the metal from ending up to the pore sidewalls in the free-standing SiN_x membranes. With the EBL approach, I could fabricate plasmonic nanopore arrays with high fabrication yield and high reproducibility.

Here in this chapter, which is based on **Paper V**, fabrication of plasmonic nanopore arrays in free-standing SiN_x membranes is described using CL and EBL methods. A series of nanofabrication techniques were employed for creating plasmonic nanostructures such as electron beam lithography, colloidal self-assembly, reactive ion etching, and electron beam physical vapor deposition, just to name a few. Herein, only the main techniques which were used for nanofabrication are described even though the fabrication and characterization processes of creating the nanostructures include many other techniques such as UV lithography, low pressure chemical vapor deposition, wet etching, ion beam milling, focused ion beam scanning electron microscopy, chemical vapor deposition, and scanning electron microscopy.

3.1 Colloidal Self-Assembly

Colloidal self-assembly or colloidal lithography (CL) exploits the nanoparticles' ability to self-assemble on surfaces, which offers a fast, cost-effective, and high throughput method to produce nanometer sized features over large surface areas (cm^2) [67]. In this work, charged colloidal particles are adsorbed to the countercharged substrate under the influence of electrostatic interactions and distributed in a random sequential process, where colloids are treated as hard spheres with an effective size that includes the Debye length [68-70]. A short-range ordered pattern is then generated, where particles are separated due to the electrostatic repulsion between the

already adsorbed and attempting-to-adsorb colloids with an average distance, depending on the Debye length [60, 62, 71].

Polystyrene beads are typically used in CL as they can be obtained in a wide variety of sizes, surface chemistries and charges [67]. Note that a clean and very hydrophilic substrate is required to obtain a high quality colloidal mask [72] . Once a uniform monolayer of colloidal nanoparticles is formed on the substrate surface, it serves as a lithographic mask during the subsequent thin film/metal deposition or ion beam milling. The colloidal particles are then removed during a lift-off process, leaving holes with desired diameter and distribution in the deposited thin films.

3.2 Reactive Ion Etching

Reactive ion etching (RIE) is a dry etching method in which the lithographically defined patterns are transferred to the underlying substrate using chemically reactive plasma [73]. Dry etching is known to make an anisotropic etch profile in contrast to wet etching which creates isotropic etch profiles. However, most conventional plasma-assisted dry etching processes (RIE) are not anisotropic and create non-vertical trenches [74]. RIE is a physical-chemical etching process which operates at relatively low pressures (from a few millitorr (mT) to hundreds of mT). Low pressure plasma reduces the scattering of ions and increases the etch directionality so that an anisotropic etch profile can be achieved [74] [75]. A variety of species are produced upon plasma ignition of a chosen gas: charged particles (ions and electrons), neutrals (radicals) and photons [75]. Since the electron mobility is much greater than the ion mobility, free electrons will quickly accelerate toward the anode and the positive ions starts drifting toward the cathode where the sample is placed. The accelerated ions will react chemically with the regions to be etched. The high energy ions also knock out the atoms from the substrate surface and thus, etching the sample physically. The highly reactive ions which react with the substrate produce volatile gases which will be pumped out of the chamber [73].

3.3 Electron Beam Lithography

Electron beam lithography (EBL) is a mask-less lithography technique which can generate nanoscale patterns with a sub-ten nm resolution [76]. In EBL, nanoscale patterns are written on an electron-beam (e-beam) sensitive resist by a highly focused electron beam. The electron beam

changes the solubility (polymer structure) of the e-beam resist so that either the exposed regions or non-exposed regions to the electron beam are dissolved in a solvent (developer) after the exposure. When the resist is strengthened by the radiation-initiated cross-linking reaction and becomes less soluble during the exposure it is referred to as negative tone resist [77]. On the contrary, positive tone resist becomes more soluble in developer and its chemical bonds (main chain and side chains) are weakened after the exposure to the e-beam so that its exposed regions are removed in the developing solution (developer).

As the electrons pass through the focusing lenses column in the EBL machine, a finely focused e-beam is formed with a diameter of a few nm [77]. When the focused e-beam strikes the resist, many of electrons experience small angle forward scattering which increases the initial beam size (also known as beam broadening). As the primary electrons slow down, much of their energy is dissipated in the form of secondary electrons. These secondary electrons are responsible for most of the actual resist exposure. As the primary electrons penetrate through the resist and move forward into the substrate, some of them experience large angle scattering and are returned back through the resist leading to the exposure of undesired areas far from the defined pattern. The backscattered electrons result in an additional exposure in the resist which is known as e-beam proximity effect.

3.4 Thin Film Growth/Deposition

Physical vapor deposition (PVD) processes or thin film processes are deposition processes in which a certain material is evaporated from a solid or liquid source in the form of atoms or molecules and transported via a vacuum or low-pressure gaseous environment to the substrate. The thickness of the thin films in PVD processes is typically in the range of a few to hundreds of nanometers [78]. E-beam PVD, is a technique in which a focused high energy e-beam is deflected onto the surface of the source material, to be melted. The melted material is evaporated and then transported in the form of vapor through a vacuum environment to the substrate and then condensed on the surface of the substrate, resulting in the film deposition [79]. In this work, Lesker e-beam evaporator was used to deposit 1 nm Cr, 30 nm Au and ~ 20 nm Al_2O_3 on the nanostructures.

3.5 Fabrication of Nanopores by Colloidal Lithography

A solid-state freestanding membrane is a prerequisite for preparing nanopore arrays. Thin SiN_x membranes are typically used for membrane pores fabrication due to their ease of preparation and relatively high stability. In this work, low stress SiN_x recipe was used to deposit 50 nm SiN_x film on both sides of 4-inch Si wafer using low pressure physical vapor deposition (LPCVD). Membrane windows with the final area of ~ 10000 μm^2 were defined in SiN_x film using photolithography (UV lithography) followed by RIE. The membrane windows in the SiN_x are then transferred to the {100} silicon (Si) substrate by the isotropic potassium hydroxide (KOH) wet etching, resulting in a freestanding SiN_x membrane on the other side of the Si support [65].

The nanopores pattern is defined on the topside of the SiN_x membrane using short-range ordered colloidal self-assembly. A few drops of 5% aluminum chlorohydrate (ACH) solution is applied to the surface prior to CL to make the negatively charged poly styrene particles adsorbed to the substrate. ACH solution is left on the surface for 1 min and then rinsed by milli-Q water. A few drops of colloidal solution should be left on the substrate for at least 4 min, followed by rinsing with water. Ethylene glycol is poured on the wafer/chips right before rinsing with water to keep the surface wet and fixing the colloids to the substrate by heating (ethylene glycol is heated up to 150 degrees prior to starting the process) [67]. The diameter of the adsorbed colloids can be modified by oxygen plasma treatment to reach a smaller diameter/size, if desired [60]. The periodicity of the final holes is determined by the characteristic distance between the neighboring colloidal particles depending on the electrostatic interactions, controlled through the salt concentration in the colloidal solution [69, 80]. The periodicity of our nanostructures, nanopores, nanocaves and nanowells, is 300 nm throughout this work. After creating short-ranged monolayer of colloidal particles with desired diameter (using oxygen plasma shrinking) on the SiN_x membranes, 1 nm Cr, 30 nm Au and 15-20 nm Al_2O_3 are deposited using electron beam physical vapor deposition (PVD). The Cr and Al_2O_3 films are utilized as an adhesion layer and a protective mask in the nanostructures, respectively. Introducing the alumina layer makes it possible to protect the underlying Au film during the lift-off and RIE [60]. The colloids covered by the Au and alumina films removed by simply rubbing them off in a liquid (water/isopropanol) using a soft material such as a finger covered by gloves or a cotton swab, which is referred to as ‘physical lift-off’. **Figure 3** illustrates the schematic view of the fabrication process using colloidal self-

assembly. Note that the process of creating SiN_x membranes is not included in the figure as it is a well-known standard process.

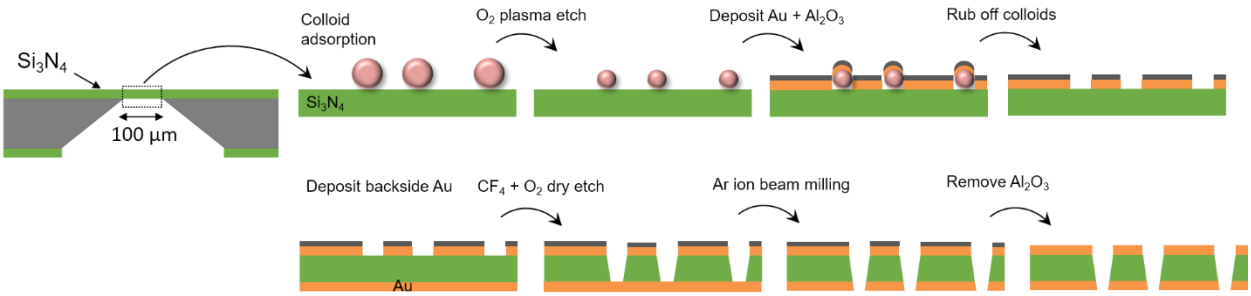

Figure 3. Fabrication of nanopore arrays penetrating the metal-insulator-metal films. Polystyrene colloids are self-assembled on a ~ 50 nm thick silicon nitride membrane, followed by deposition of the top metal layer and an alumina film. After removing the colloids, 30 nm Au film is deposited on the membrane backside, followed by dry etching, ion milling and removing the alumina layer.

The array of nanopores is then transferred to the SiN_x membrane using RIE when the structures with only single Au film is required. In case of double Au films, where the SiN_x membrane is sandwiched between the two Au films, another layer of Au is deposited on the backside of the membrane before etching the SiN_x membrane. Afterwards, the nanopores pattern is transferred to the SiN_x membrane and the backside Au film using RIE and Ar ion beam milling, respectively. The Al_2O_3 layer acts an excellent mask not only during the RIE but also during the ion beam milling due to its relatively low sputtering rate.

The results of the nanofabrication process are summarized in **Figure 4**. The arrays of nanopores in free-standing SiN_x membrane was imaged by scanning electron microscopy (SEM). **Figure 4A** shows SEM images of the backside of the SiN_x membrane windows, imaged from the Si side. **Figure 4B** and **4C** demonstrate the top view SEM images of the short-range ordered arrays of nanopore in metal-insulator-metal (MIM) films with diameter of 150 nm and 70 nm respectively.

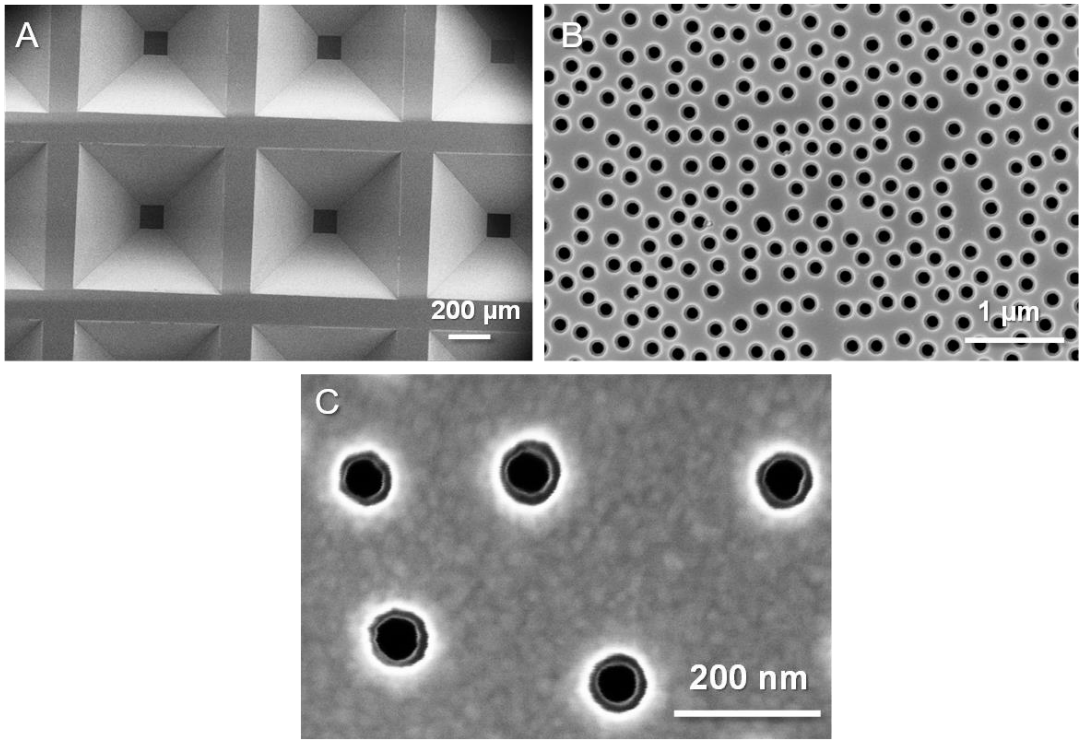

Figure 4. SEM images of nanopores in silicon nitride membranes with double gold films; **(A)** Arrays of membranes supported by the silicon wafer imaged from the backside **(B)** Example of ''larger'' nanopores (diameter of ~ 150 nm) imaged from the topside **(C)** Close up showing ''smaller'' nanopores (diameter of ~ 70-80 nm) imaged from the topside. Note that the backside diameter is also visible (Figure and caption from **Paper II**).

The nanofabrication method (using colloidal lithography) described above is compatible with parallel processing of multiple membranes on the same chip and also on the whole 4-inch Si wafer. However, the yield of the fabrication process in terms of the intact membranes after the lift-off is typically 25%, implying that only one membrane out of four on each chip remains intact after the lift-off; the exact fabrication yield depends on the membrane inherent mechanical stress. Moreover, it becomes increasingly difficult to remove smaller colloids (with diameter of 80 nm for instance) from the membrane without breaking it as a higher mechanical force is required to remove them from the membrane. To increase the yield of fabrication, we developed a new CL method where the lift-off is performed on the whole wafer before creating the membranes.

In the new approach we perform CL, metal deposition and physical lift-off, before forming the SiN_x membranes (before etching the Si support using KOH). After lift-off, the whole wafer is spin coated by a photoresist (S1813) to protect the Al_2O_3 and Au films during the KOH wet etching, in which the membranes are formed. It is critical that the topside of the wafer is fully covered and

protected by the resist as contact with concentrated KOH will destroy the nanostructure. This requires a thick protective layer which at the same time should be possible to remove in the subsequent development or oxygen plasma steps. After creating the SiN_x membranes by KOH, the protective resist is fully removed using a solvent (AR 300-76). The arrays of nanopores in Au film are then transferred to the underlying SiN_x membrane using RIE if nanopores with only single Au film is desired. Otherwise, another Au deposition is performed on the backside of the membranes, followed by RIE and Ar ion beam milling. **Figure 5** shows a schematic view of the fabrication process of the nanopore arrays with single Au film with the new approach, where the key step is to use a protective resist during the wet etching of the Si substrate.

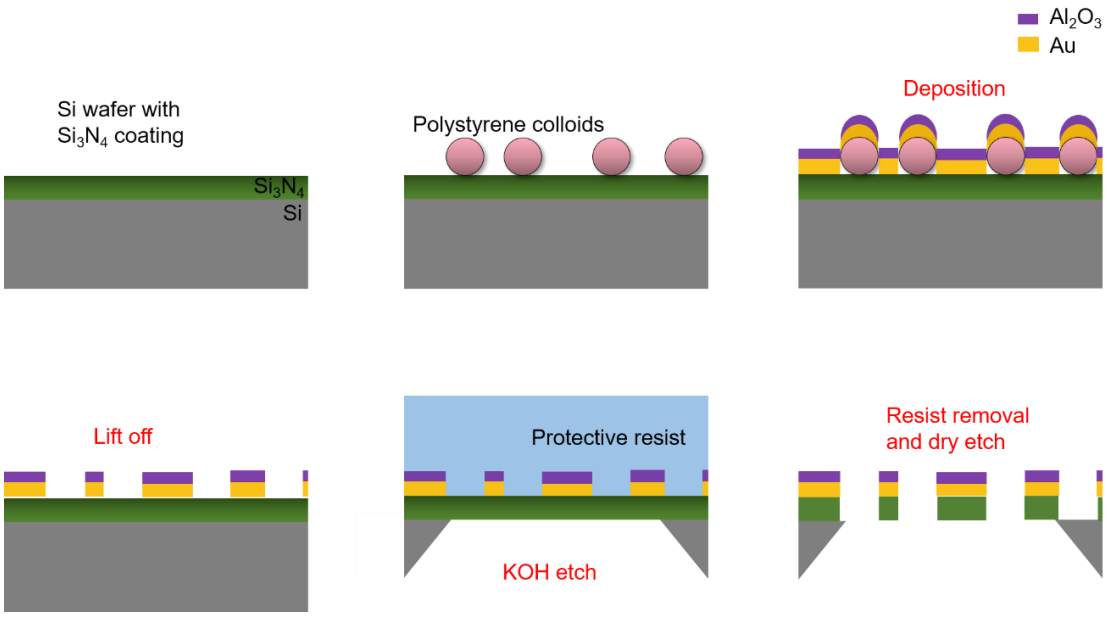

Figure 5. Fabrication of plasmonic nanopore arrays by CL with using a protective resist; making nanopores in the Au film before forming the silicon nitride membrane. Colloidal particles are self-assembled on ACH-modified silicon nitride film, followed by gold and alumina thin films deposition. After physical lift-off, the wafer is spin-coated with photo resist (protective mask), followed by KOH etching of the Si wafer to form the silicon nitride membrane. After forming the membrane, resist is removed, followed by dry etching (figure from **Paper V**).

To summarize, we have developed arrays of nanopores penetrating suspended MIM films by short-range ordered colloidal self-assembly with two different approaches. The majority of the membranes remain intact in the CL approach where the protective resist is used during forming the SiN_x membranes. However, the reproducibility of the method is limited with the perfect coating of the wafer's top surface with the photoresist. Therefore, to achieve a high yield of

nanofabrication process specifically when the smaller pores are required, we used electron beam lithography to prepare nanopore arrays in MIM films

3.6 Fabrication of Nanopores by Electron Beam Lithography

Herein the EBL approach is described for fabrication of plasmonic nanopore arrays in optically thin SiN_x membranes. The fabrication of free-standing SiN_xmembranes has already been explained in the previous sections. In the EBL approach, the chips containing SiN_xmembranes or the whole 4-inch wafer are spin-coated with the negative resist ma-N 2403 (cyclopentanone and anisole). Of note, Ti prime (2-methoxy-1-methyl ethyl acetate and 2-metoxipropylacetate) was spin coated at 3000 rpm for 20 s as an adhesion layer prior to the resist coating. Only the membrane area (typically 100 × 100 μm^2), is exposed to the electron beam during the lithography. The nanopore arrays pattern is written by a highly focused electron beam on the e-beam sensitive resist using 100 kV electron beam machine (JEOL JBX 9300FS). Since we have used negative-tone resist, the exposed areas to the e-beam are strengthened and thus the non-exposed regions are dissolved in a solvent during the subsequent development process. As a result, the arrays of 'pillars' on the SiN_x membranes emerge after the development (Ma-D 525 containing tetramethylammonium hydroxide) procedure. By fine-tuning parameters such as resist thickness and the electron dose we could achieve arrays of highly vertical pillars with the height of ~ 300 nm. **Figure 6A** shows a top view SEM image of arrays of negative resist pillars patterned on SiN_x membranes. **Figure 6B** illustrates a SEM tilted view of the pillar arrays covered with Au and alumina before lift-off, at the edge of the pattern.

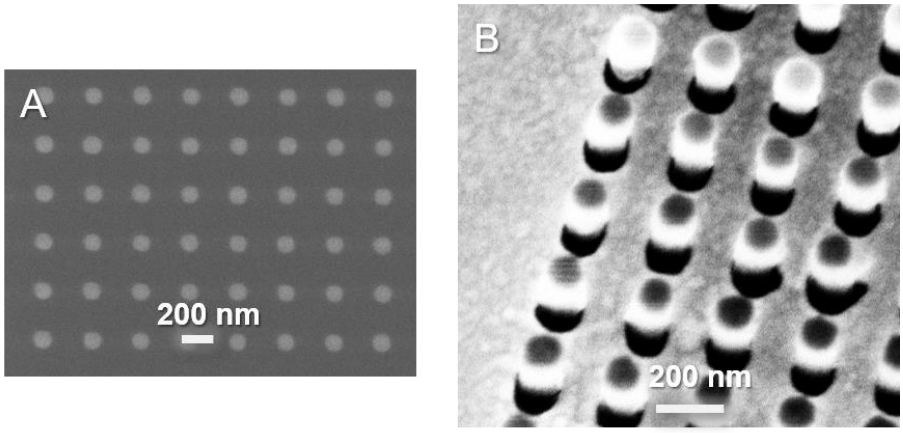

Figure 6. SEM characterization of the pillar arrays after EBL **(A)** Top view after development **(B)** Tilted view after metal and alumina deposition.

Note that the entire 4-inch Si wafers were processed at once, with writing speed of thousands of pillars per second resulting in an efficient patterning. **Figure 7** presents a 4-inch Si wafer including SiN_x membranes from the backside, where the Si has been etched to form the SiN_x membranes. It shows an arbitrary design of the chips and membranes, where the membrane windows inside the chips appear grayish.

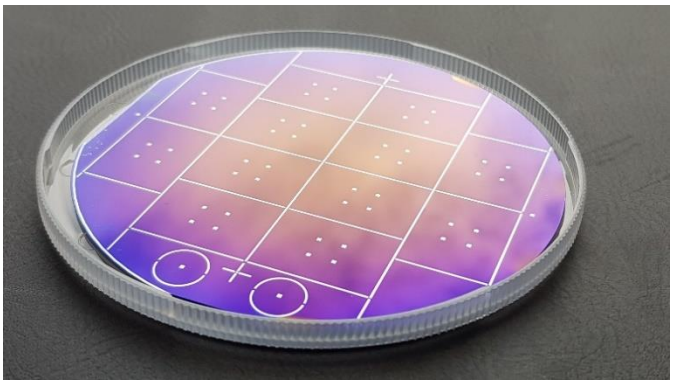

Figure 7. A 4-inch Si wafer containing rectangular and circular chips with silicon nitride membrane patterns, after UV lithography and RIE.

A schematic view of the fabrication process of nanopore arrays with double Au films using EBL is presented in **Figure 8**. After development step, the arrays of pillars are coated by 1 nm Cr, 30 nm Au and 20 nm Al_2O_3 using e-beam PVD (The thickness of the Al_2O_3 layer can be increased up to at least 30 nm without influencing the result). After metal deposition, the pillars coated with

metal are removed by a chemical lift-off process, leaving nanopores in the Au film (note that the process of lift-off together with its challenges are extensively discussed in the next section). The pores are then transferred to the free-standing SiN_xmembranes using RIE if the structure with single Au film is required.

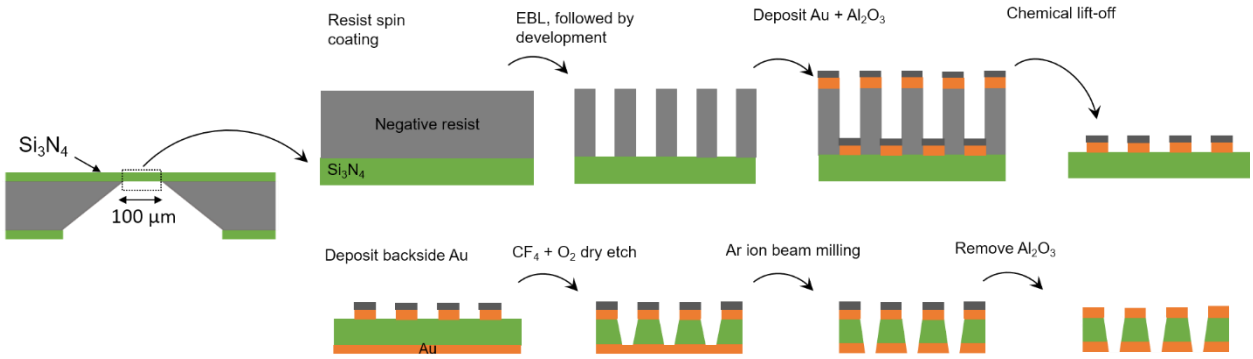

Figure 8. Schematic of fabrication process of plasmonic nanopore arrays penetrating MIM films using EBL with negative resist. After development, the pillars are coated with Au and alumina (dark grey), followed by chemical lift-off. The backside gold (orange) is deposited, followed by dry etching and Ar ion beam milling of the backside gold film.

Figure 9A presents the top view SEM image of a SiN_x membrane after patterning and metal deposition. The long-range ordered nanopore arrays with single Au film with diameter of ~150 nm is shown in **Figure 9B** and **9C**. The shape of the apertures in structures with single Au film (**Figure 9C**) is as close to circular as expected for polycrystalline gold [81].

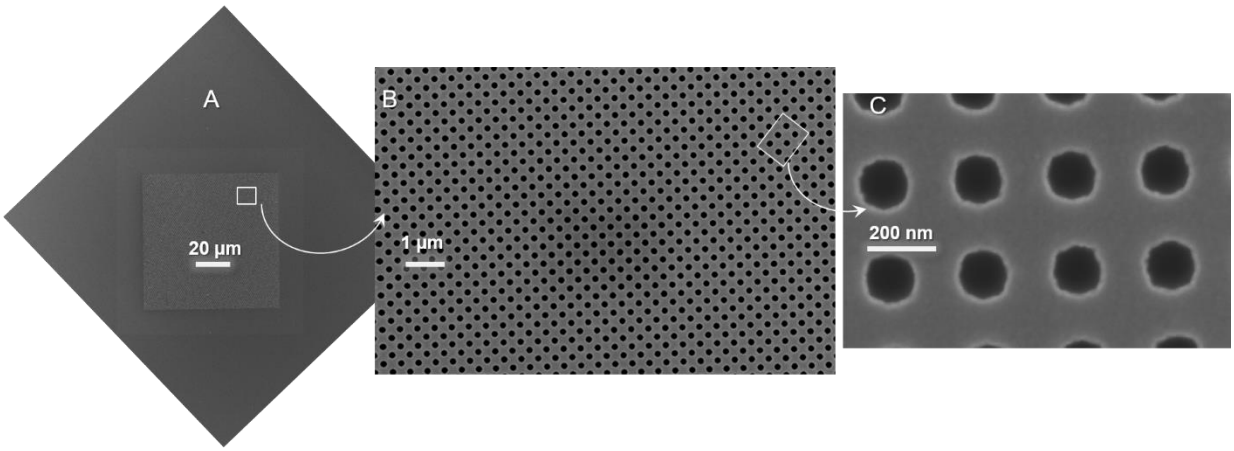

Figure 9. Top view SEM images of **(A)** Si-supported silicon nitride membrane patterned with e-beam nanopores **(B)** Nanopore arrays in silicon nitride membrane with single gold film **(C)** Closeup of figure (B).

When the structures with double Au films are required, another 30 nm gold film is deposited on the backside of the SiN_x membrane before the dry etching step. The arrays of nanopores in the MIM films are created by etching the underlying SiN_x membrane and the backside Au using RIE and Ar ion beam milling, respectively. Since the dry etching is not entirely perpendicular to the surface, the interior walls of the nanopores are slightly inclined. The inclined walls in the entire structure are more pronounced in the structures with double Au films as the Ar ions should reach the backside Au film through the top apertures. For instance, there is a ~ 50 nm differences in diameter of the pores, between the topside and the backside of the structures with double Au films.

Electron microscopy characterization of the nanopore arrays with double Au films are shown in **Figure 10(A-D)**. The nanopores were found with diameter and periodicity of ~ 150 nm and 300 nm, respectively. The diameter distribution of the long-range ordered nanopores is presented in **Figure 10F** which indicates 10 nm variation in diameter of the pores. The diameter of the pillars could be tuned down to ~ 70 nm, at which point the pillars started to collapse during the development process due to a high aspect ratio. Smaller diameters could potentially be achieved by tuning the electron dose and/or the resist thickness. **Figure 10C** shows nanopores arrays in MIM films with diameter of ~ 80 nm. A cross-section SEM image of the nanopores in MIM films is presented in **Figure 10D,** indicating no metal residues on the silicon nitride walls in the nanopores interior.

We have analyzed and compared the radial distribution functions (RDF) of the nanopores prepared by EBL and CL methods, shown in **Figure 10E.** There is a 300 nm peak in the RDF of the nanopores prepared by CL, which indicates the characteristic spacing in the short-range ordered pattern. The EBL pores exhibit the same long-range period as CL pores but with more peaks in the RDF, indicating other lattice vectors.

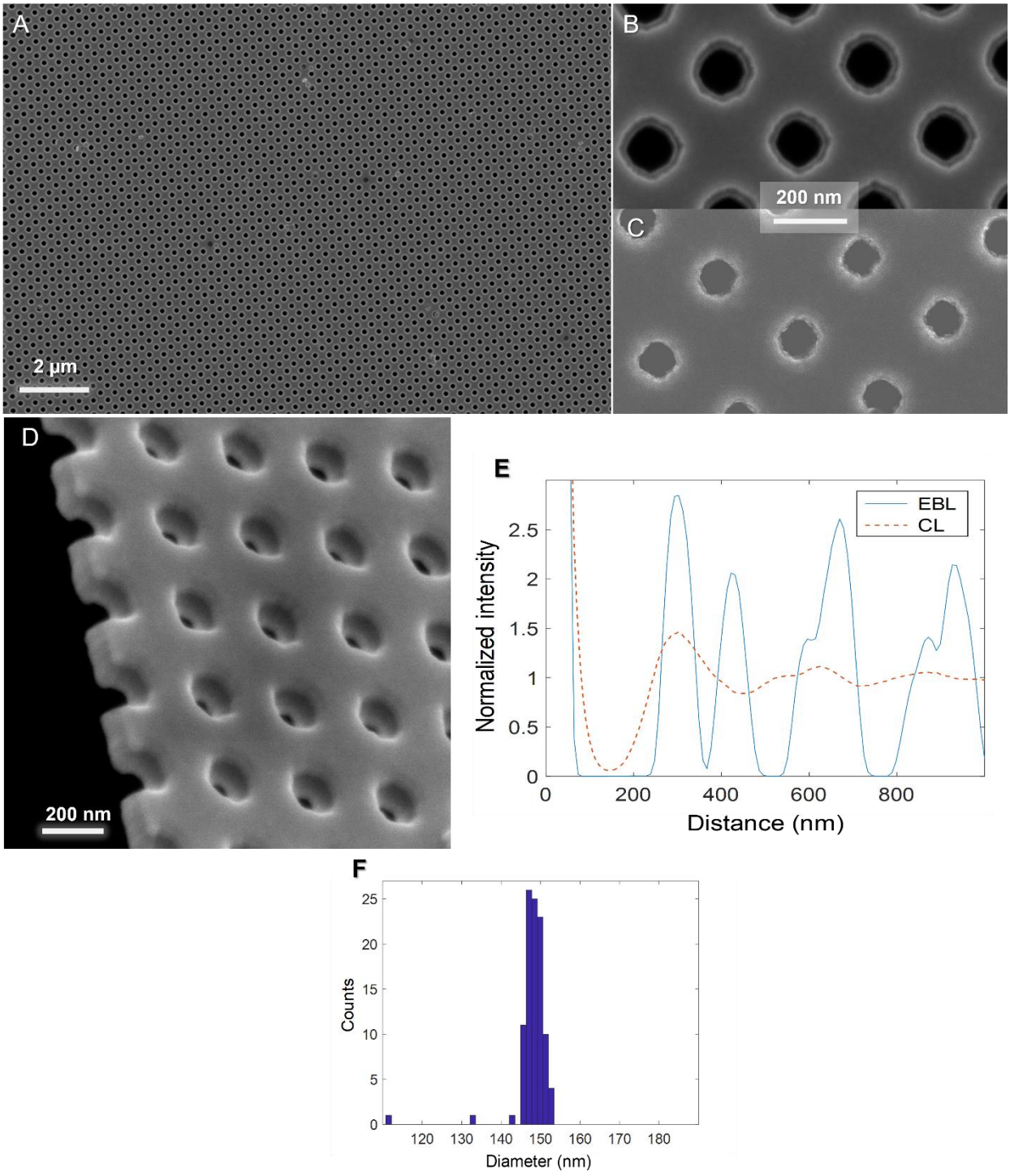

Figure 10. Electron microscopy characterization of plasmonic nanopore arrays with double Au films **(A)** Long-range ordered nanopore arrays in MIM films **(B)** Higher magnification of nanopore arrays with diameter of 150 nm **(C)** Close up of smaller nanopores with dimater of 80 nm **(D)** Cross-section of nanopores with double gold films, showing no metal residues in the pore sidewalls in silicon nitride **(E)** Radial distribution functions of EBL pores and CL pores **(F)** Example histogram of aperture diameter of 150 nm pore arrays with single Au film (figure from **Paper V**).

By employing EBL with using negative resist, we have developed well-ordered array of nanopores in MIM films while most of the SiN_x membranes remain intact. In addition to achieving a high fabrication yield in terms of number of intact membranes, EBL allows to have a better control on the nanopores arrangement (diameter and periodicity) in each membrane over the 4-inch Si wafer. Employing negative resist made it possible to avoid metal residues from ending up to the membrane pores sidewalls as the pores were constructed in the Au film before forming the membranes. With our method, long-range ordered arrays of nanopores with plasmonic functionality were fabricated in SiN_x membranes in a well-controlled and highly reproducible manner. This provides the opportunity to compare the optical properties of long-range ordered arrays of nanopores with their short-range ordered counterparts (**Paper V**).

3.6.1 Lift-Off Challenges

I have used negative resist to create membrane nanopores, as mentioned in previous sections. One of the known challenges with negative resists is pillars with inclined walls after development. However, the exposure of the e-beam resist on ~ 50 nm thick SiN_x membranes, results in highly vertical negative resist pillars after the development as the effect of backscattered electrons and hence proximity effect becomes negligible on such a thin SiN_x substrate. Due to transparency to electrons, optically thin SiN_x membranes are utilized in transmission electron microscopy, known as TEM windows [82, 83]. **Figure 11** shows SEM images of collapsed pillars after development (**Figure 11A**) and after lift-off (**Figure 11B** and **11C**) respectively which clearly indicates highly vertical pillars with no inclined side walls. If the pillars were inclined (if the thickness of the pillar increases from top to the base) instead, the lift off process would become challenging or even impossible as the metal (Au in this case) is deposited not only on the top of the pillars but also on the pillar walls, and hence connecting the metal on top of the pillars to the deposited gold film in between the pillars. In that case, solvent/developer cannot reach the resist during the lift off as the pillars are fully covered with the metal. However, creating pillars with straight side walls eliminates the risk of covering pillars with metal and hence makes it possible to perform lift-off process.

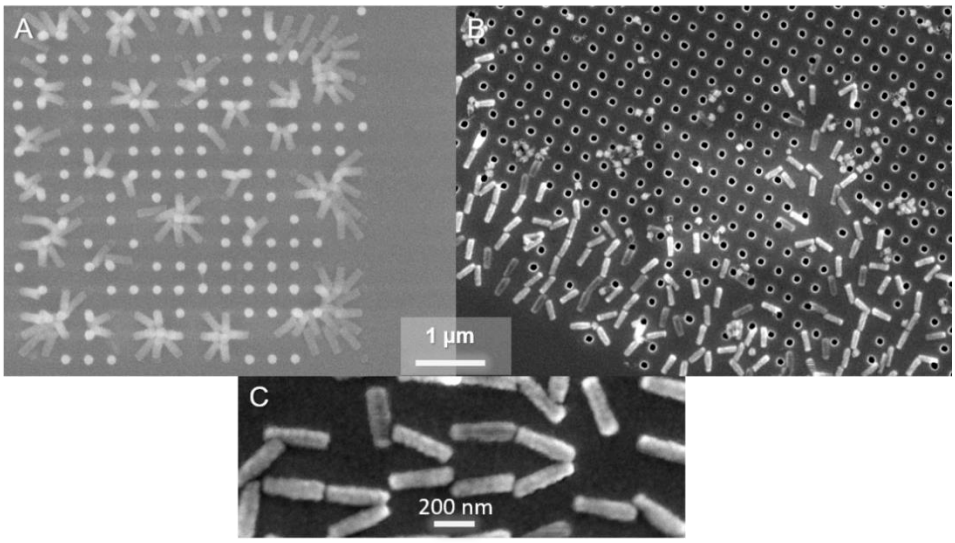

Figure 11. SEM images of collapsed pillars after **(A)** Development **(B)** and **(C)** After lift-off**.** The collapse of the pillars is occurred due to their high aspect ratio at a certain electron dose (A and B from supporting information of **Paper V**).

Another critical step to achieve an effective lift-off in our work is to prevent the metal on top of the pillars from landing on the membrane top surface. Otherwise, nanopore defect sites or so-called metallic caps, block some of the pores which in turn affects flow through pores in further experiments and also changes the plasmonic properties**.** Note that the metallic caps include not only the metal but also a thin layer of alumina on top. **Figure 12** shows SEM images of poor lift-off, where metallic caps landed on the membrane surface.

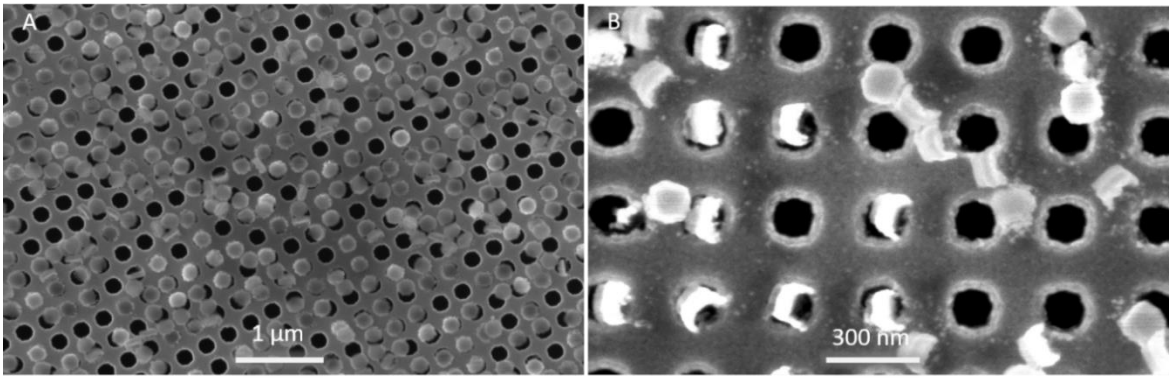

Figure 12. SEM images of membrane nanopores with poor lift-off **(A)** Single Au film **(B)** Double Au films.

After several tentative attempts, the desired lift-off was achieved when the wafer was positioned with the exposed side facing down in the remover (Mr-rem 700 solvent containing ethanolamine) under gentle agitation. Ultrasonic agitation, which is common in lift off process, was avoided to prevent breaking the SiN_x membranes. The agitation was performed instead by creating a constant stirring of the remover at 300 rpm using a magnetic stir at ~ 50 °C. With this approach we could achieve high-quality lift-off with a reasonable reproducibility. **Figure 13** demonstrates SEM images of high-quality lift-off, where only very few metallic caps (~ 1% compared to the number of pores) were found.

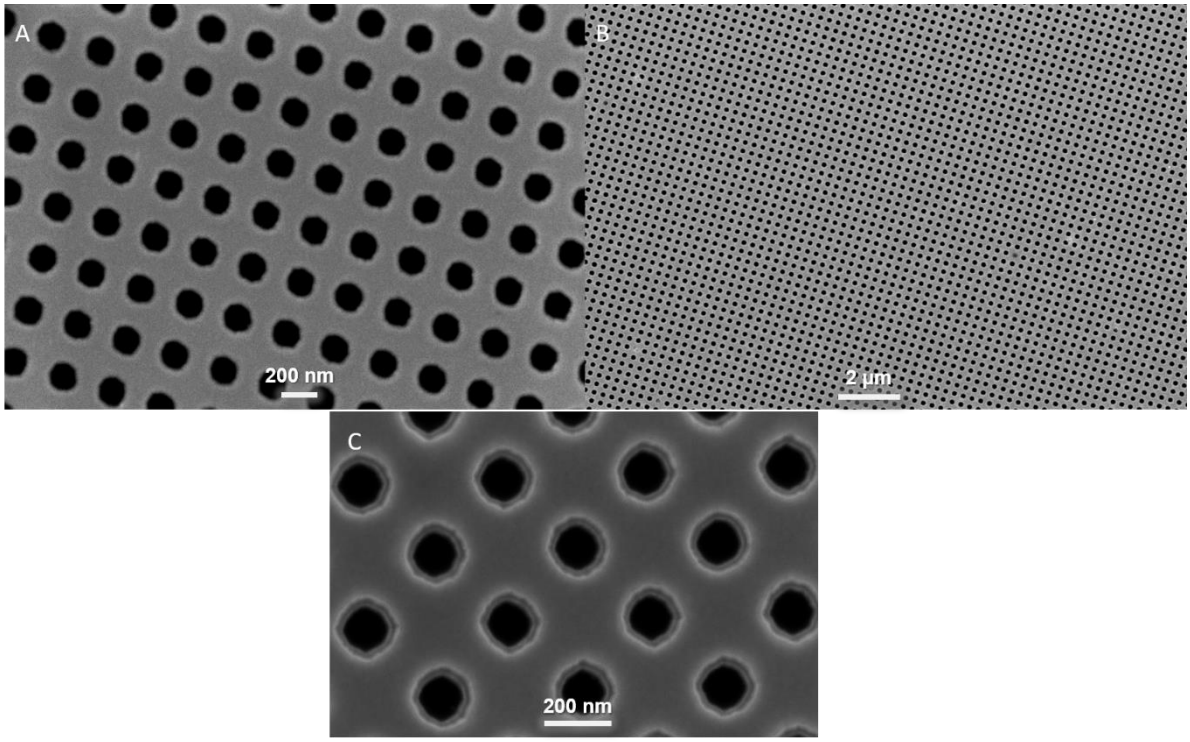

Figure 13. SEM images of membrane nanopores after lift-off **(A)**, **(B)** After RIE **(C)** After ion beam milling.

4

Fabrication of Plasmonic Nanocaves and Nanowells

In this chapter, plasmonic nanoscale cavities in solid support denoted as ‘nanocaves’ and ‘nanowells’ are introduced. I have prepared nanocave and nanowell arrays using short-range ordered colloidal self-assembly. The main difference in the fabrication process of the nanocaves and nanowells is the degree of the anisotropy of the etching of the solid support underneath of the nanoholes array. The fabrication process is briefly explained here as the full description can be found in **paper I**.

Clean fused silica (amorphous SiO_2) and regular glass substrates are used for preparing nanowells and nanocaves, respectively. The silica supports should be treated with oxygen plasma since a surface modification is required to make the silica substrates hydrophilic for CL. The CL process is the same process as performed for preparing nanopore arrays on silicon nitride membranes, described in the previous chapter. **Figure 14** illustrates the schematic of the fabrication process for preparing plasmonic nanocaves and nanowells using short-range ordered colloidal self-assembly.

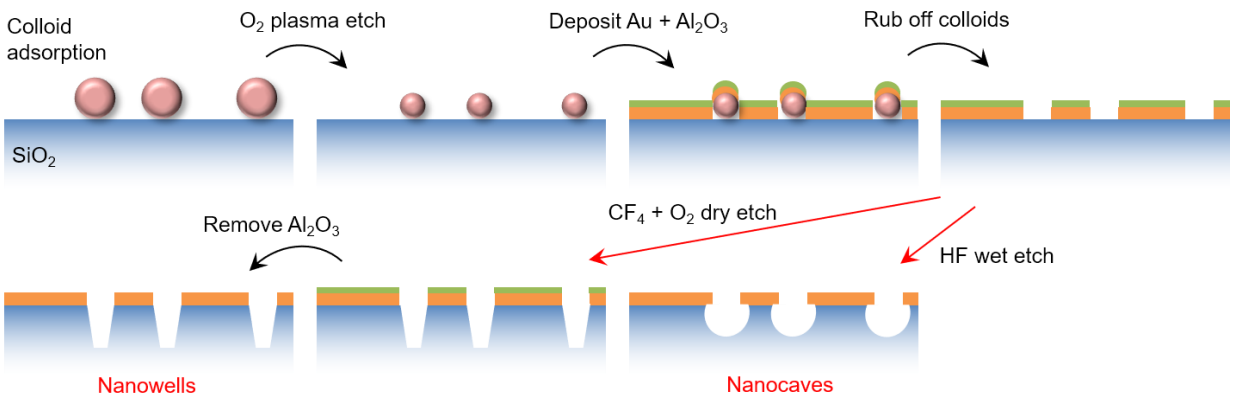

Figure 14. Schematic of fabrication process for preparing 'nanowells' and 'nanocaves'. Colloidal lithography was performed to create nanoholes array. After physical lift-off, two different etch processes are used to make different nanostructures. Anisotropic dry etching is used to create nanowells while more isotropic wet etching is used to make nanocaves. The alumina layer (green) is removed in the HF wet etching during preparation of the nanocaves, but it does not affect the Au film (orange) (Figure from **Paper I**).

After performing CL, the size of the adsorbed colloids can be modified using oxygen plasma to define the diameter of the final cavities. After reaching a desired diameter of the adsorbed colloidal particles, 1 nm Cr, 30 nm Au and 15 nm alumina are deposited using e-beam PVD. The colloids covered by the gold and alumina films are then removed by physical lift-off (rubbing them off from the surface in a liquid, water/isopropanol, using a soft material).

After lift-off, the underlying substrate is anisotropically etched employing RIE using CF_4 and O_2 for creating nanowells. The flow ratio of the CF_4 and O_2 was 4:1 during the RIE. The power and pressure were 50 W and 15 mT respectively to achieve a relatively high etch rate for SiO_2 (almost 20 nm/min depending on the chamber condition and equipment). The Al_2O_3 layer is then removed by any weakly basic solution (such as 30 mM NaOH) to expose the gold film for further experiments [84].

For creating nanocaves, isotropic wet etching with hydrofluoric acid (HF) was used to etch the underlying support creating a half sphere-like shape void in the SiO_2 substrate. In this way, using wet etching of SiO_2 substrate, each nanoscale aperture in the planar gold film is transformed to a nanocave in a free-standing gold layer. The etch rate was found to be relatively high (almost 160 nm/min for 6% HF concentration). The alumina film is removed during the wet etching process

while the Au film remains intact [85]. The etch rates presented here were estimated based on measuring the depth of the nanowells and nanocaves for three different etching times.

The geometry of nanocaves and nanowells was characterized by SEM and focused ion beam scanning electron microscopy (FIB-SEM). **Figure 15B** shows top view SEM images of the nanocaves with a closeup in **Figure 15A**. The top view of nanocaves and nanowells appear identical when imaged by SEM, except that for nanowells it is possible to see that the walls in the underlying cavities are slightly inclined. It is important to visualize the shape of the cavities for both structures in the SiO_2 support as the structures should be particularly useful to address nanoscale geometry-related questions [12]. FIB-SEM was employed to perform cross-sections, thereby revealing the structure of the nanoscale cavities. **Figure 15 (C-E)** shows cross-section images of the nanowells and nanocaves, obtained by FIB-SEM. A single nanocave cross-section image is shown in **Figure 15E** (right).

It should be noted that there is a small increase in the average diameter of the nanowells, typically 10 nm, after 5 min RIE due to reactions with the exposed Au film. **Figure 15 (C-E)** demonstrate that the sidewalls of the nanowells in SiO_2 are almost vertical with a slight inclination on the walls towards the center, representing that the bottom of the nanowells is slightly smaller in diameter than the top apertures regardless of the gas ratio, power, and pressure during the RIE. The maximum depth of the nanowells was 200 nm, measured by atomic force microscopy (AFM).

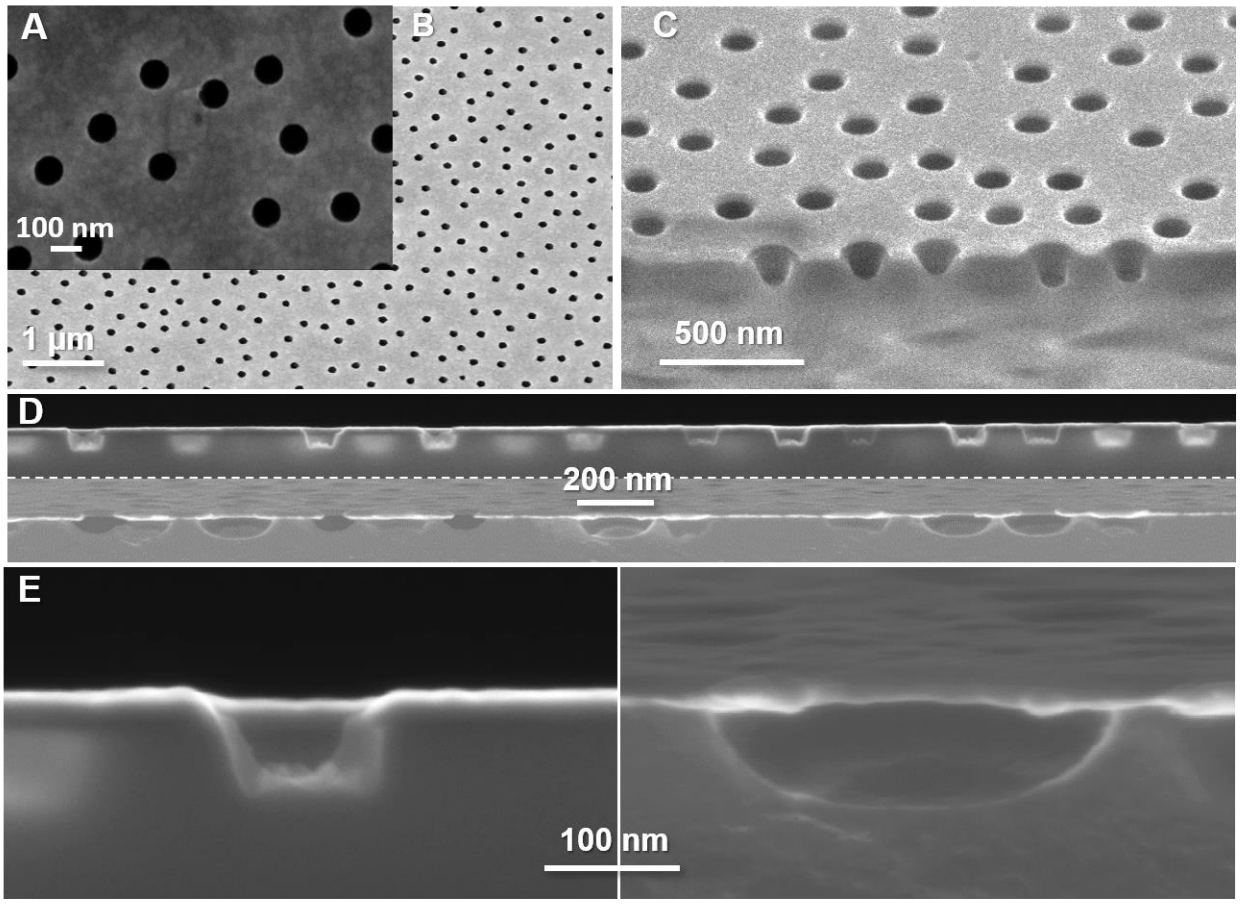

Figure 15. Electron microscopy characterization of nanostructures. **(A)** Zoomed-in top view of nanocaves; **(B)** Top view of nanocaves; **(C)** Nanowells imaged with tilt at a location for FIB analysis; **(D)** Sideview of cut samples (nanowells in top and nanocaves in bottom image); **(E)** Closeups showing the cross-section geometry of a nanowell (left) and a nanocave (right). Note that these images are just examples, i.e., different samples are shown so the diameter and depths are varying (Figure and caption from **Paper I**, except image **(A)**).

The cross-section images of the nanocaves reveal an isotropic etch profile as expected. The depth of the caves is not equal to the etch undercut (the depth is almost 100 nm while the undercut is almost 50 nm) representing a 'semi-isotropic' etch profile **(Figure 15D and 15E)**. Since there is an aperture of exposed SiO_2 surface when the wet etching starts, the depth of the cavity would be larger than the etch undercut, so the cavity is not expected to be a perfect half-sphere. This influences how large nanocaves that can be prepared. If the caves start to connect laterally underneath of the gold film due to the excessive etch undercut, the structure collapses. So, it is important to consider the etch undercut length when designing the diameter of the nanoscale apertures for preparing nanocaves.

5

Optical Properties of Plasmonic Nanostructures

The optical characterization of plasmonic nanostructures with different architectures is presented in this chapter. Plasmonic behavior and spectral analysis of subwavelength holes periodically arranged in solid supports are discussed in detail (**Paper I and V**). We have also made a comparison between the optical properties of the long-range ordered and short-range ordered nanopores in freestanding MIM films.

5.1 Extinction Spectra of the Nanocaves and Nanowells

It is well established that the periodic patterned metal films with subwavelength periodicity enables excitation of SPs by grating coupling mechanism under visible light illumination [80]. For thin Au films, SPs excitation by aperture periodicity is manifested in the far field as a maximum (peak) in the extinction spectrum, while a minimum (dip) appears at a nearby longer wavelength due to associated localized resonance (**Figure 16**). Note that the extinction (absorption + scattering) spectrum is the logarithm of the inverse of the transmittance of light through the nanoscale apertures. The short-range ordered arrays of nanocaves and nanowells exhibit the characteristic asymmetric resonance (a peak and a dip) in the their extinction spectra, associated with this kind of periodic apertures in thin Au films [8, 84]. **Figure 16** illustrates the extinction spectra of nanocaves and nanowells in air and water, representing the characteristic surface plasmon resonance spectral features.

Although the resonance spectral features (peak and dip in the extinction spectra) cannot be treated independent of one another, it is still possible to analyze their respective response to certain parameters such as aperture shape or the characteristic distance between the apertures, so-called

periodicity. Since the resonance arises from the grating-coupling mechanism, the extinction peak position depends on the periodicity and on the thickness of the Au film. The resonance peak wavelength however, does not strongly depend on the pore diameter as that parameter is not relevant for the resonance condition [60].The transmission maximum or the extinction dip, however, is sensitive to the shape of the apertures and thus behaves like a localized resonance with its field more focused to the interior of the pores [80]. If there is a change in the shape of the apertures one can expect a shift almost solely in the dip resonance wavelength when the periodicity and the Au film thickness are constant [80].

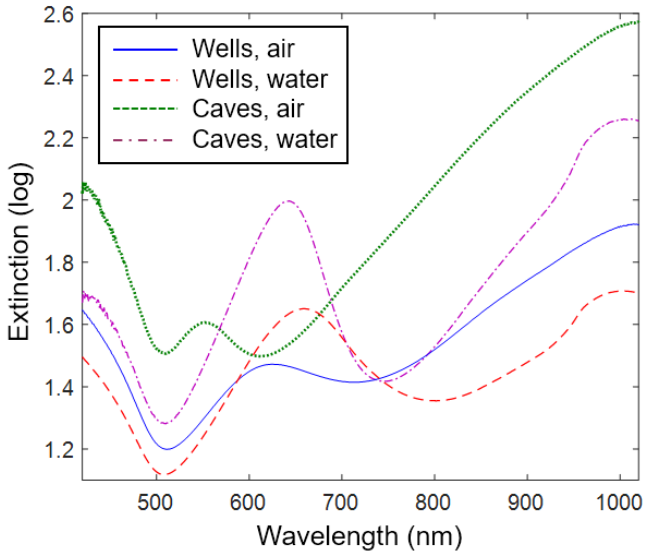

Figure 16. Extinction spectra of nanowells and nanocaves in air and water. The nanowells were 150 nm deep and 120 nm in diameter. The nanocaves were 70 nm in diameter and 100 nm deep. The periodicity of the nanostructures is 300 nm. The small increase in extinction at 980 nm in water is due to water absorption (figure and caption from **Paper I**).

The extinction spectrum of the plasmonic nanocavities is sensitive to the refractive index (RI) of their nanoenvironment. For instance, when the SiO_2 support is partly removed for preparing nanocaves and nanowells, the RI decreases and thus the peak and dip positions in the extinction spectra are blue shifted, compared to ordinary nanohole arrays [60]. It should be kept in mind that the plasmon resonance condition only depends on the RI of the environment when the aperture arrangement and the Au film thickness are kept constant. The extinction peak and the dip in **Figure 16** are red shifted when the medium in contact with the nanoplasmonic structures is altered from air to water, due to the increase in the refractive index of the environment.

By creating cavities in the SiO_2 support, the refractometric sensitivity of the nanowells and nanocaves is increased as a larger volume of liquid is present close to the metal, where changes in RI due to molecular binding can occur. Herein, the sensitivity of the nanoplasmonic sensors is defined as resonance spectral shift per RI change in the liquid. For nanocaves, the lateral etching under the Au film increases the liquid probing volume and therefore, enhances the sensitivity compared to nanowells. Etching the SiO_2 support also increases the field strength on the topside of the Au film, leading to further sensitivity enhancement. We measured the sensitivity of the plasmon resonance for 100 nm deep nanocaves and nanowells using glycerol/water mixtures. Of note, the periodicity (300 nm) and the thickness of the Au film (30 nm) is the same and kept constant for both structures. The peak sensitivity for nanowells and nanocaves was 147 nm and 294 nm per RI unit respectively, shown in **Figure 17**. The etch undercut in nanocaves results in a higher sensitivity in the extinction dip as well, compared to nanowells. According to the sensitivity measurements in **Figure 17**, the extinction dip sensitivity for nanocave and nanowells were 388 and 278 nm per refractive index unit, respectively. Although the values obtained for the dip sensitivity is higher than the peak sensitivity for both structures, one must also consider other factors about which parameter (peak or dip shifts) to use for refractometric sensing. For instance, dip is a more broadened spectral feature causing a higher noise level. Another important factor is the field extension with respect to the thickness of the layer of molecules bound to the sensor surface as the field extension strongly influences the magnitude of the plasmonic signal [86]. For nanocaves and nanowells, the field extension at the peak wavelength is mainly determined by the thickness of the gold film. For the dip wavelength however, the field is more focused to the interior of the cavities (localized resonance mode) so the molecules should bind to the interior of the cavities to achieve a high signal at the dip wavelength.

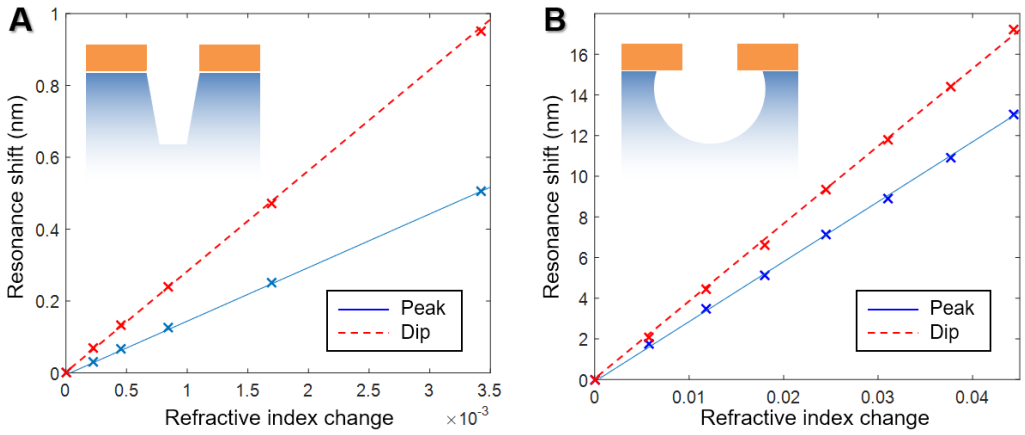

Figure 17. Refractive index sensitivities of **(A)** nanowells and **(B)** nanocaves. Both structures show linear sensitivities from pure water (1.33) up to at least 1.4. For these experiments, the nanowells were 150 nm deep and 120 nm in diameter. The nanocaves were 70 nm in diameter and 100 nm deep (Figure and caption from **Paper I**).

5.2 Location-Specific Detection using Nanowells and Nanocaves

Here in this section, the sensing application of the plasmonic nanowells and nanocaves is briefly presented. **Figure 18** shows a schematic of nanowells and nanocaves, where first short (2 kDa) chains of thiolated poly(ethylene glycol) (PEG) is grafted to Au, making it inert towards the subsequent protein adsorption [10]. The sensor response to molecular adsorption was characterized by the adsorption of the protein avidin inside the nanocavities. The centroid shift for both peak and dip of the plasmonic spectra upon thiolated PEG grafting and also avidin adsorption are shown in **Figure 18** [12]. All the measurements were performed in PBS buffer solution and all binding was irreversible. In this experiment, thiolated PEG solely binds to the Au film and avidin binds only to SiO_2 inside the cavities (**Figure 18B**) since PEG prevents avidin from adsorbing to the Au film. These material-specific reactions provide the opportunity to not only detect molecular binding events but also to assess the sensitivity distribution in the nanostructures.

As can be seen in **Figure 18A** nanocaves provide a higher plasmonic signal for adsorption to Au, since there is more Au surface available for PEG to bind and also the plasmonic field is higher on the top surface away from the SiO_2 substrate. However, nanocaves provide more moderate signal upon protein binding to SiO_2 cavities even though they have a higher SiO_2 surface area available compared to nanowells. This can be explained by the fact that the SiO_2 walls in nanocaves are not

close to the rim of the cavities where the sensitivity is highest (see the optical field simulations for nanowells in Figure 2 in **Paper IV**). Since the metal film structure (such as film thickness, diameter of the cavities and periodicity) is almost identical for the nanocaves and nanowells, we believe the optical field simulations in **Paper IV** for nanowells are still applicable for nanocaves. In contrast, nanowells provide a relatively high dip shift upon protein binding to the SiO_2 cavities. This indicates that the ideal nanostructure for the refractometric sensing, depends on which material in the sensor is chemically modified for binding a target.

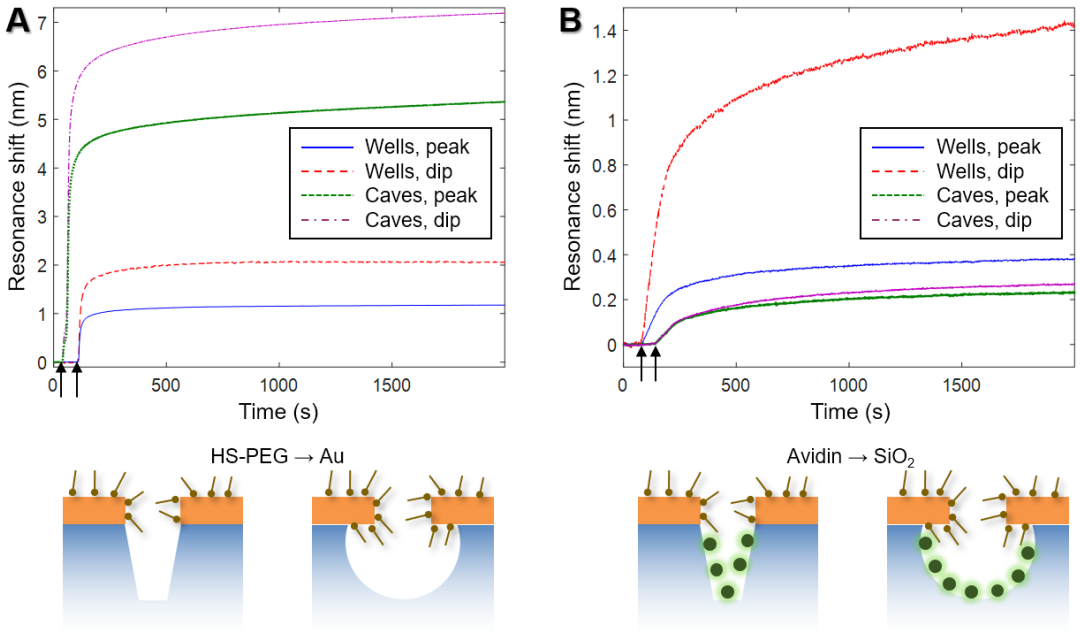

Figure 18. Real-time plasmonic response from location-specific molecular binding to the nanostructures; **(A)** Thiolated 2 kDa poly(ethyleneglycol) binding to Au; **(B)** Protein adsorption to the silica cavities. The temporal resolution is 250 ms and the data is not smoothened. The nanowells were 120 nm deep and 100 nm in diameter. The nanocaves were 70 nm in diameter and 100 nm deep. (Figure and caption from **Paper I**).

The dip to peak ratio of the resonance shift for both nanostructures in **Figure 18** is always higher than one and a higher value for this ratio demonstrates binding to the interior of the cavities [12]. For nanocaves the dip to peak shift ratio is 1.3 for Au and 1.2 for SiO_2, Indicating that the ratio does not change so much when looking at the material specific binding (see **Figure 18**). However, for nanowells the ratio is 1.8 for Au and 3.7 for SiO_2 representing that nanowells provide a higher ratio when comparing binding inside the cavities and to the planar top surface. In other words, nanowells show a clear spectral signature of preferential binding inside the cavities, when looking

at the location-specific detection. This demonstrates how full spectral analysis can qualitatively provide information about the location-specific binding.

5.3 Optical Properties of Freestanding Nanopore Arrays

There is a strong interest to understand the optical properties of subwavelength aperture arrays in thin metal films and how the ordering of the structurally identical nanopores influences their optical response [62, 87-90]. As discussed previously, periodic nanostructures in thin metal films can generate surface plasmon resonance by interacting with visible light through a grating-coupling mechanism. Plasmonic properties of aperture arrays in thin metal films have been extensively investigated. However, literature is inconsistent with respect to the spectral identification of localized and propagating surface plasmon modes [8, 61]. Preparing structurally identical structures, where the only difference between the structures is the aperture ordering makes it possible to better understand their plasmonic response, specifically with respect to the nature of their far field spectral features. Our novel EBL approach using negative resist, allows the precision required to vary only the ordering in the structures. Herein, we discuss the optical properties of the long-range ordered and short-range ordered membrane pore arrays in continuous metal films prepared by EBL and CL methods.

Figure 19 illustrates SEM cross-section images of short-range ordered and long-range ordered membrane pore arrays. As described in previous chapters, the long-range ordered array of nanopores was fabricated in a 30 nm Au film, penetrating in the 50 nm thick SiN_x membrane using EBL. The structurally identical nanopores with short-range ordering were created by colloidal self-assembly with periodicity of 300 nm. The structures were made with two different diameters of 150 nm and 80 nm in both lithography methods, referred to as larger and smaller pores in this section.

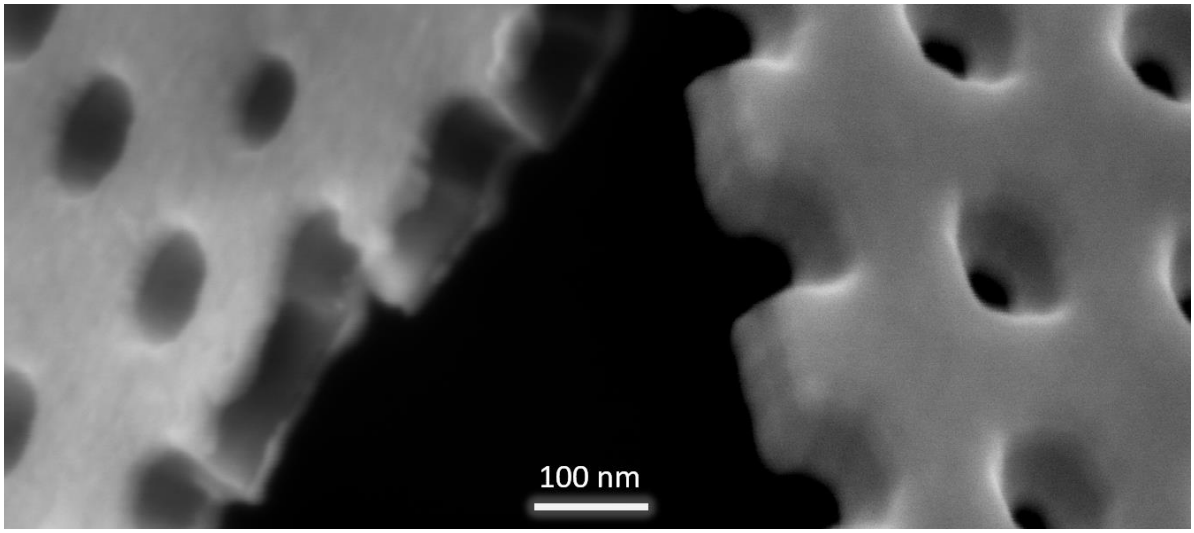

Figure 19. SEM cross-section images of CL (left, taken from reference [65]) and EBL (right) pores in 50 nm thick silicon nitride membrane with double Au films.

The periodic nanopore arrays in metal-insulator or metal-insulator-metal films, demonstrate the characteristic resonance spectral features of grating coupling excitation. **Figure 20** shows the representative extinction spectra of long-range ordered and short-range ordered nanopores with single Au film (**Figure 20A**) and double Au films (**Figure 20B**). The spectral features in the extinction spectra in **Figure 20** are signature of the interaction between the periodic nanopores and visible light. Regardless of whether the structures have short-range or long-range order, the asymmetric resonance features from the nanopore arrays consists of a peak (transmission minimum) and a dip (transmission maximum) at a nearby longer wavelengths [61, 91]. It can be clearly seen in **Figure 20** that the peak and dip positions are red shifted upon increasing the refractive index of the surrounding medium; from air to water. The increase in the extinction spectra in the blue region and near infrared region is due to the gold absorption and higher reflectivity, respectively [60, 92]. The presented extinction spectra in **Figure 20** corresponds to the membrane pores with diameter of 150 nm. The optical results were highly reproducible as the optical measurements were performed on several chips (typically ~ 10) for all structures; the variation in the peak wavelength was within 10 nm for different chips.

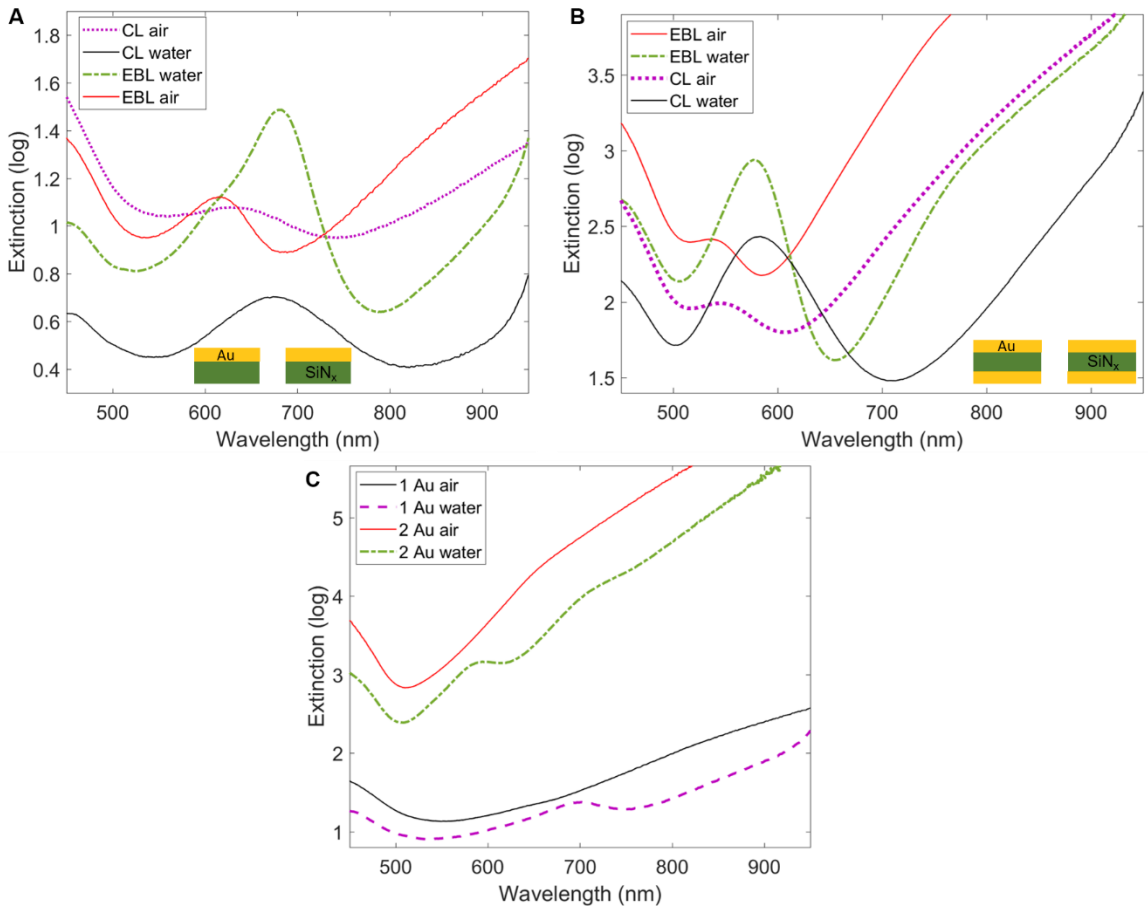

Figure 20. Extinction spectra of membrane nanopores fabricated by EBL and CL methods, with **(A)** single Au film and **(B)** double Au films. **(C)** Comparing the extinction spectra of EBL pores with diameter of 80 nm with one or two gold films in air and water (Plots from **Paper V**).

From comparing the extinction spectra of EBL pores and CL pores in **figure 20**, it turns out that the peak is slightly higher in magnitude for the EBL pores as there is more efficient light coupling to surface plasmons due to the perfect ordering of the apertures. Moreover, the extinction minimum is blue shifted by tens of nm compared to their CL pores counterpart. Note that all the CL pores presented in this section were made by a new CL approach (described in paper V), representing a very similar optical response to the CL pores fabricated by the old method [60]. **Figure 20C** shows a comparison between the extinction spectra of the EBL pores with single or double Au films, where the diameter is reduced from 150 nm to 80 nm. Just like for CL pores, this size shrinking results in a remarkably reduced peak magnitude in water while the resonance features disappear entirely in air. Complementary optical images of the EBL pores patterned at the center of the

membrane under transmission illumination as well as dark field images of the EBL pores and CL pores are shown in **Figure 21B.**

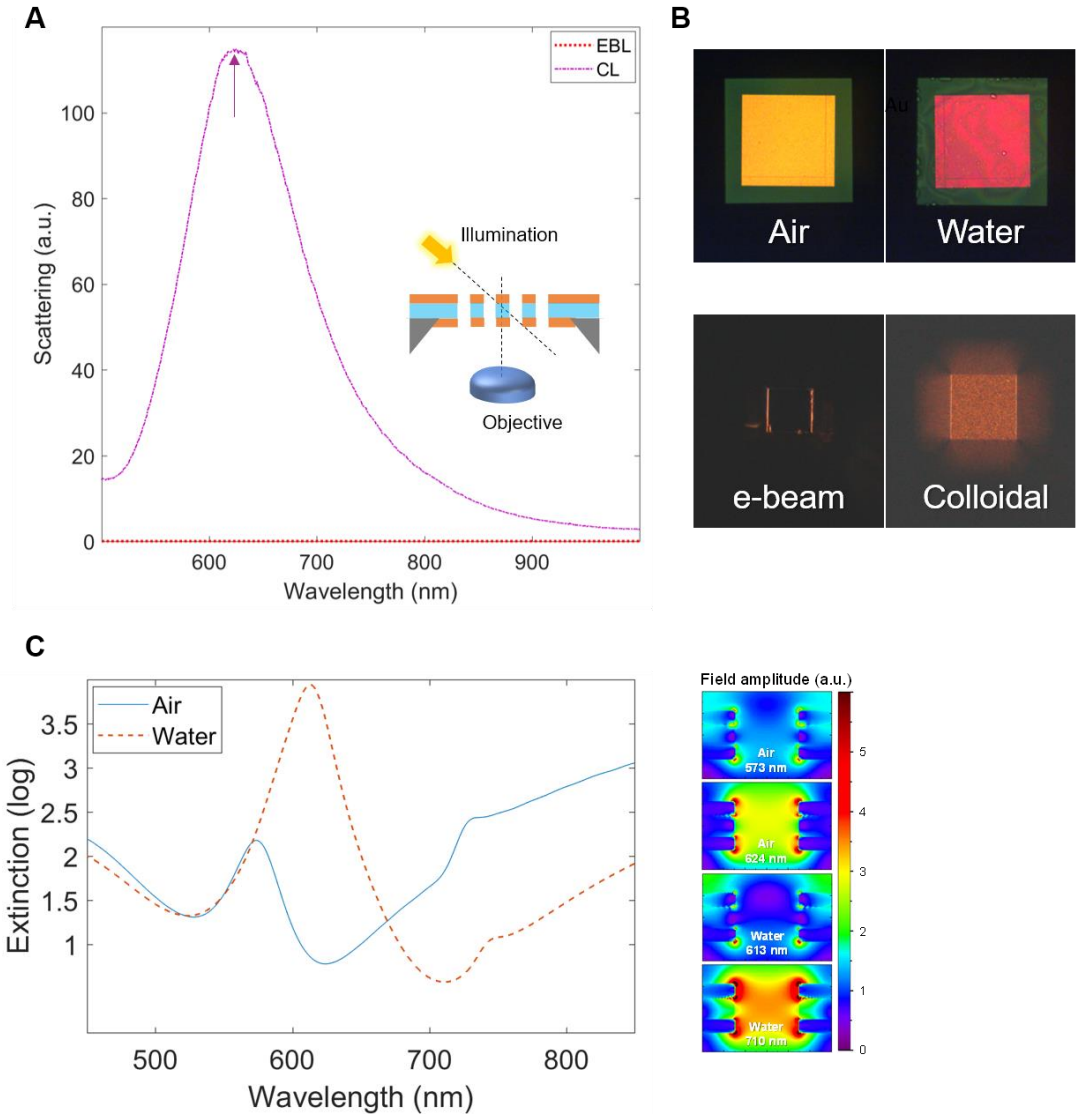

Figure 21. (A) Scattering spectra from double gold films EBL and CL pores in air with diameter of 150 nm **(B)** Optical camera photos of EBL pores (top images in air or water) under transmission illumination and dark filed images of CL and EBL pores with double Au films (lower images, EBL or CL pores). The membranes are approximately 100 × 100 μm^2. **(C)** FDTD simulations of 150 nm pores with double Au films in air and water, including near-field plots at the extinction maximum and minimum (Figure and caption from **Paper V**).

The optical response of EBL pores and short-range ordered arrays (CL pores) are very similar, but when going into details several differences emerge. Single nanoholes in optically thin metal

films are known to exhibit resonant scattering [93, 94]. **Figure 21A** and **21B** show the scattering response of the short-range ordered *vs.* long-range ordered arrays of nanopores. A strong resonant light scattering was observed for CL pores while the long-range ordered arrays only support the 0^{th} order diffraction. All other scattering angles than zero becomes suppressed due to the destructive interference between scattering from the pores in a perfectly ordered array with subwavelength periodicity [95]. For CL pores however, when the long-range ordering is perturbed, the short-range ordered arrays no longer suppress the non-zero angle scattering through destructive interferences.

CL pores with double Au films exhibit stronger scattering, at least twice as much, compared to single film CL pores which can be explained by stronger resonance as there are more pronounced distinct resonance features for CL pores with two gold. The stronger resonance scattering for double Au films CL pores may also be attributed to the role of the nanopores structure in the interplay between the metal absorption and scattering as the two different possible paths for SPP decay [96]. It has been shown that even long-range ordered arrays with comparable diameter and periodicity exhibit scattering but then the whole array is size-limited (a few micron) [97]. Similarly, scattering can occur at the edges of the EBL array where the periodicity is interrupted, as shown in **Figure 21B**.

Extinction peak position appears at the same wavelength for EBL pores as for the CL pores, regardless of the refractive index of their surrounding environment or whether the structures are with single or double gold films. However, the dip in the extinction spectra is consistently blue shifted for EBL pores, compared to CL pores (**Figure 20**). In previous works, the extinction dip or the transmission maximum was attributed to the localized resonance mode as the dip is very sensitive to the changes in the pores shape and diameter which is the characteristic behavior of localized resonance mode [62, 91]. Further, the extinction dip exhibits a stronger field enhancement inside the pores compared to the transmission minimum, as confirmed by finite-difference time domain (FDTD) simulations, see **Figure 21C**. The picture of the spectral resonance features (transmission minimum and maximum) can be even made more generic: It has been demonstrated that the whole spectral features of the long-range ordered arrays can be explained by Fano interference between the broad transmission through individual pores in thin films and grating-coupling to the propagating surface plasmons [93, 94, 98]. Short-range ordered arrays can

be expected to exhibit similar behavior (Fano-shaped profile), only with less efficient grating coupling to the propagating surface plasmons and consequently broader spectral features. In fact, weakening the resonance strength and broadening the linewidth of the Fano-shaped spectra results in less steep resonance features and larger spectral distance between the peak and the dip for CL pores. Consequently, the blue shift in the extinction dip for the EBL pores is consistent with the Fano model as there is less efficient resonance coupling to the continuum background (transmission through individual pores) for the short-range ordered arrays [98].

The scattering maximum for double gold films CL pores appears near the extinction dip which slightly differs from the literature for single film short-range ordered arrays where the resonant scattering lies approximately in the middle between the extinction peak and dip [69]. According to the Fano interference, the plasmon resonance position, if defined based on the simulated maximum absorption, should appear somewhere in between the transmission peak and dip. Evan. *et al*. have used the Fano approach and demonstrated that the plasmon resonance position is expected to coincide with the extinction peak for optically thin films (semi-transparent films) and with the extinction dip for thick nanohole films [98]. When the direct transmission is high (*e.g.* for smaller periodicity, larger diameter, or thinner films) the plasmon resonance position is expected to lie close to the extinction peak, whereas it is expected to appear closer to the transmission peak for the case of lower direct transmission (*e.g.* larger periodicity, smaller diameter, or thicker films). For CL pores with double gold films, since the direct transmission is lower than the structure with single gold film, the resonance position is expected to appear closer to the extinction dip which agrees with our experimental results.

6

Nanoplasmonic Biosensors

Nanostructured plasmonic sensors offer a label-free platform to study the influence of nanoscale geometry on biomolecular interactions. Nanoscale membrane curvature is known to play an essential role in biochemical processes [12, 99-101]. One can utilize the unique advantage of nanoplasmonic sensors over conventional SPR, the nanoscale geometry of the sensor, to address nanoscale curvature-related issues. Here in this chapter, sensing applications of our novel nanoplasmonic sensors are presented. We have employed plasmonic nanowells (with two architectural configurations) to investigate the influence of nanoscale curvature of a model biological membrane on protein binding (**Paper III**, and **Paper IV**). Further, we have utilized plasmonic nanopore arrays for location-specific detection of proteins (**Paper II**). Besides the label-free real-time detection, nanopores also offers the opportunity of mimicking biological nanomachines when size of the nanopores approach ~ 50 nm.

6.1 Plasmonic Nanowells Detects Preferential Protein Binding to Negative Membrane Curvature

We have utilized nanowells as a label-free nanoplasmonic biosensor, to detect preferential protein binding to negative membrane curvature (**Paper IV**). Nanowells were coated by a conformal layer of lipid bilayer membrane using vesicle fusion to investigate the influence of membrane curvature on protein binding via spectral analysis of the plasmonic response. We have studied the protein IRSP53, containing I-BAR domain which is believed to be a curvature-sensitive protein [102]. The I-BAR domain in the IRSP53 protein interacts with negatively charged lipids in the membrane and induce cell membrane deformation [103, 104]. Of note, plasmonic nanowells provide information about preferential binding, but not if the protein induces curvature in the membrane, leading to membrane deformation. IRSP53 binding in physiological ionic strength (150 mM) was confirmed

by quartz crystal microbalance with dissipation monitoring (QCM-D) and found to be irreversible upon rinsing. At higher ionic strength, the protein was released upon rinsing indicating the electrostatic nature of the interaction. In most of the experiments, the behavior of the IRSP53 was studied at physiological ionic strength.

Two different types of plasmonic nanowells were used in terms of the materials in the structure: one structure with silica (SiO_2) underneath the Au film and the other one with niobia (Nb_2O_5) on a borosilicate support. The schematic of plasmonic nanowells with two different configurations is shown in **Figure 22A**. Fabrication process of SiO_2 nanowells using short-range ordered colloidal self-assembly has been already described in chapter 4 (**Paper I**). Nanowells with the additional layer of niobia were prepared by sputtering niobia on borosilicate substrate [12]. The aperture diameter in gold is ~ 100 nm for both structures. The thickness of the gold film and niobia is 30 nm and 200 nm, respectively.

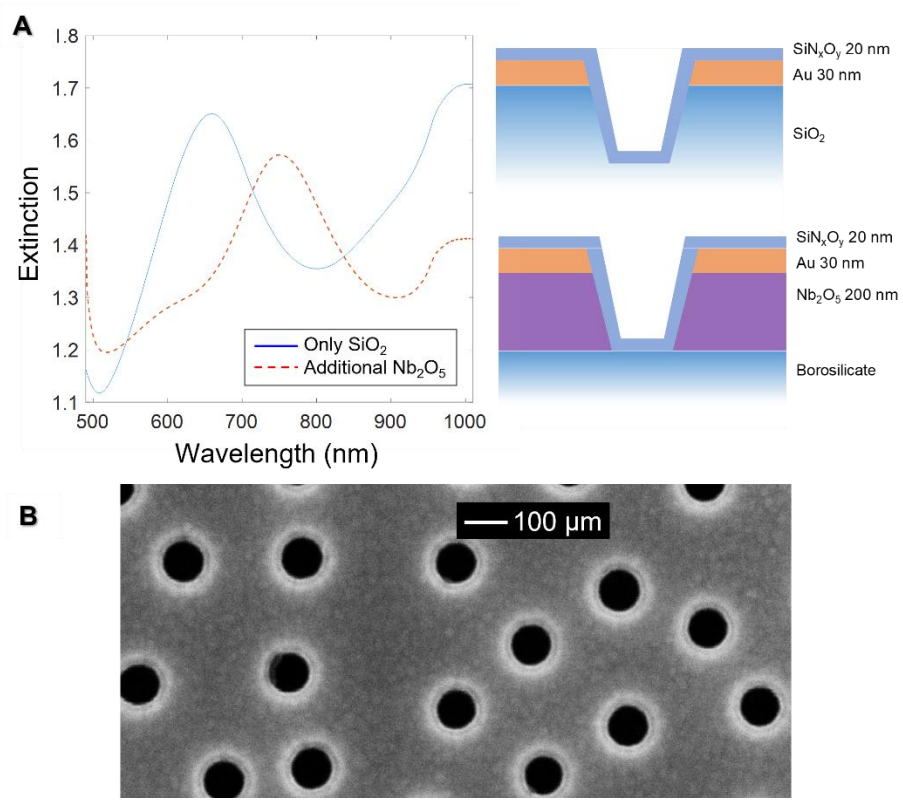

Figure 22. Plasmonic nanowells with two different configurations **(A)** Extinction spectra in water and schematic of silica nanowells and niobia nanowells with specified film thicknesses **(B)** Top view SEM image of silica nanowells after silicon nitride coating (Figure from **Paper IV**).

Prior to all experiments, a conformal layer of silica or silicon nitride with thickness of ~ 20 nm was deposited on the nanowells using plasma enhanced chemical vapor deposition (PECVD). This insulating coating could not be fully visualized by SEM. However, a reduction in diameter of the apertures after deposition was observed in SEM when imaging from above, shown in **Figure 22B**. Oxygen plasma treatment was performed to clean the sensors prior to bilayer formation. So, the silicon nitride coating is expected to include a significant fraction of oxygen with unknown stoichiometry (SiN_xO_y).

Figure 22A shows the characteristic extinction spectra of the short-range ordered nanowells [12]. The asymmetric plasmon resonance (peak and dip) of niobia nanowells appear at a longer wavelength compared to silica nanowells as niobia has a higher refractive index (2.2) than silica (1.5) [12]. As discussed in chapter 5, the resonance features in the extinction spectra behave differently in refractometric sensing; the extinction dip behaves as a localized resonance while the extinction peak position corresponds to the grating-type excitation of propagating surface plasmon mode [60]. Considering the origin of the resonance features in terms of surface plasmon modes, location-specific detection becomes feasible by proper spectral analysis. Relative shifts in the extinction peak and dip wavelengths, can provide information about preferential binding to negative curvature, i.e., the tendency of proteins to bind to the interior of the membrane-coated nanowells.

In order to analyze the degree of affinity to negative membrane curvature in a quantitative manner, a dimensionless parameter ζ is defined as follows [12]:

$$\zeta = 1 - \frac{\Delta\lambda_{peak}}{\Delta\lambda_{dip}} \qquad (7)$$

Since the extinction dip has a higher sensitivity upon changes in refractive index than the extinction peak, ζ is always larger than zero [12, 60]. For binding to the planar surface, $\Delta\lambda_{peak}$ can be as high as $\Delta\lambda_{dip}$ so that ζ approaches zero. For binding inside nanowells instead, $\Delta\lambda_{peak}$ can be close to zero so that ζ approaches one [12].

Figure 23 shows the near field simulations at the extinction peak and dip wavelengths for both niobia and silica nanowells, in fair agreement with the experimental data in **Figure 22A**. Note that the difference in the simulated peak (820 nm) for niobia nanowells arises from the fact that the

periodicity of the niobia nanowells was 230 nm in the experiments while the simulated values is based on the periodicity of 300 nm. The near field plots illustrate which regions of the nanowells are most sensitive to the changes of the refractive index. It is clear from the simulated near field that the field is stronger at a lower side of the gold film for niobia nanowells as the niobia has a higher refractive index compared to silica. It is clear from the simulations in **Figure 23** that the average field strength is higher for the silica nanowells compared to the niobia nanowells. The bar plots in **Figure 23** illustrate that although the field is stronger inside the nanowells at both peak and dip wavelengths, the ratio of the peak and dip field strengths is higher inside the nanowells compared to the top planar region which is the basis of our location-specific detection concept for nanowells.

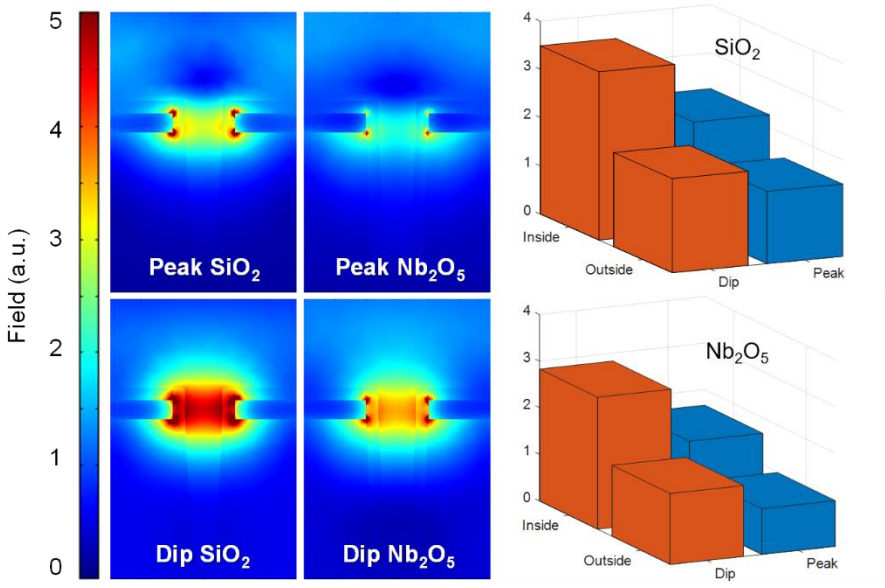

Figure 23. Simulated near fields of the nanowells (cross-section view) at the extinction peak and dip wavelengths for square arrays with periodicity of 300 nm in water. The bar plots illustrate the average field strength on the planar surface (out of the wells) vs. the interior of the nanowells, in both cases 5 nm away from the silicon nitride coating (which has a refractive index 1.5) (figure from **Paper IV**).

Supported lipid bilayer formation on silica-based materials is a well-known procedure that occur upon vesicle adsorption and a subsequent vesicle rupture on the substrate [105, 106]. Bilayer formation on nanowells was confirmed by QCM-D and also by nanoplasmonic sensing (for details see **Paper IV**). We first introduced a protein without any curvature preference, NeutrAvidin, to the bilayers containing a small fraction of biotinylated lipids in order to establish a reference value

for ζ. **Figure 24** shows plasmonic response upon introducing NeutrAvidin on both silica and niobia nanowells. The corresponding value for ζ is 0.4 for those experiments which is in agreement with previous results on similar niobia nanowells showing 0.5 ± 0.1 [12]. In our measurements, the variation in ζ remained below 0.1 after repeating the measurements with the same structure.

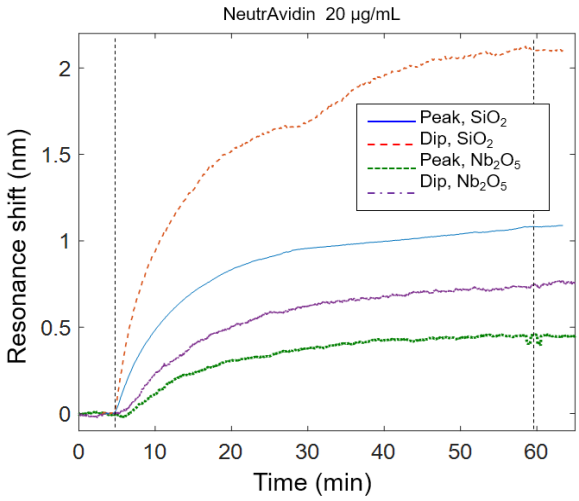

Figure 24. Resonance shift upon NeutrAvidin binding on nanowells coated with membrane-containing biotinylated lipids in real-time. Extinction peak and dip are monitored for both silica and niobia nanowells (Figure from **Paper IV**).

After verifying the bilayer formation and obtaining the values for ζ upon binding of NeutrAvidin as a protein with no surface curvature preference, we monitored the resonance shift upon introducing a curvature-sensitive protein, IRSP53, to bilayer-coated nanowells. **Figure 25A** shows plasmonic response upon IRSP53 binding at two different concentrations. The dip vs. peak shifts upon IRSP53 binding to lipid membrane-coated nanowells for several experiments are shown in **Figure 25B and 25C**. One can obtain information about the curvature preference of the protein during the binding process from the shape of these plots (dip vs. peak shifts). Note that since the bilayer is a 2D liquid environment, the bound protein molecules have the possibility to diffuse and find the nanoscale geometry that they prefer to bind. Further, the IRSP53 concentration should be kept low enough, to avoid saturation to enable the detection of preferential binding. Otherwise, proteins also bind to the planar membrane when the whole surface of the sensor is saturated resulting in a different slope in the peak vs dip plots compared to low concentrations of IRSP53. If the target protein has the tendency to bind to negative surface curvature (inside the nanowells), the dip should increase faster initially, before surface saturation occurs. Thus, curvature preference

can be identified early in the binding process. **Figure 25D** shows the dip vs. peak ratios for IRSP53 binding and also NeutrAvidin binding to membrane-coated niobia nanowells. As expected, the plots are linear for NeutrAvidin as it is not a curvature-sensitive protein and non-linear for IRSP53 binding (early in the process and at low concentrations).

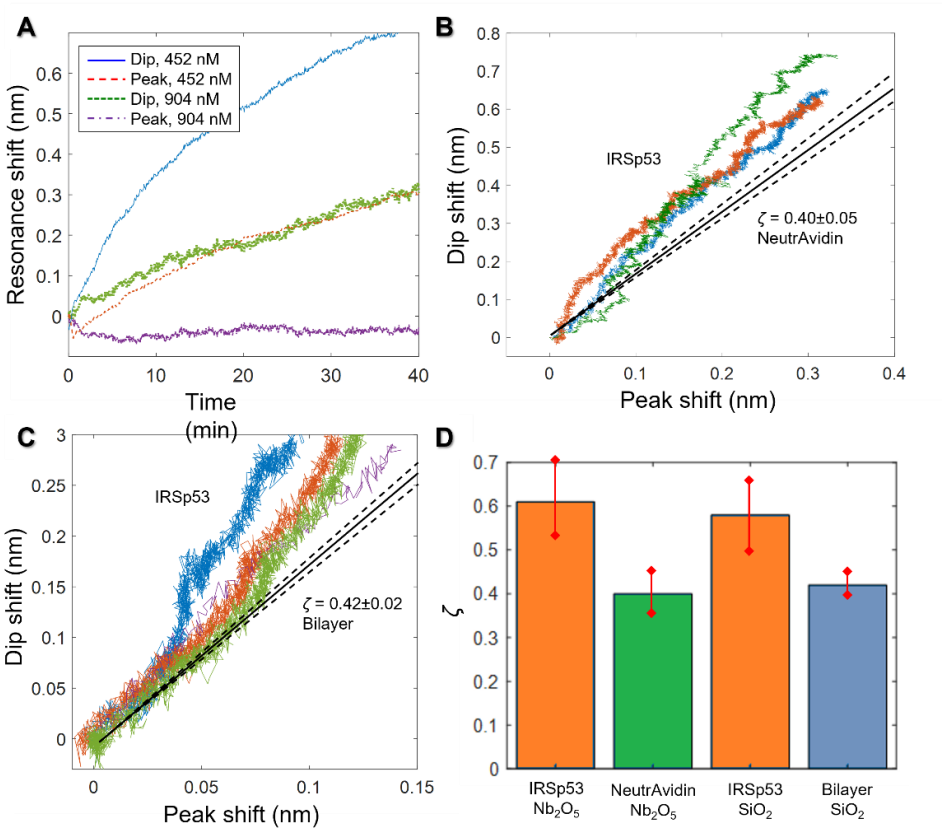

Figure 25. IRSP53 binding with negative curvature preference **(A)** Resonance shift upon IRSP53 binding to membranes containing negative lipids on niobia nanowells at two different concentrations. For the lower concentration no peak shift is observed. **(B)** dip vs. peak shifts for IRSP53 and for NeutrAvidin binding to membrane-coated niobia nanowells **(C)** dip vs. peak shifts for IRSP53 binding to membrane-coated silica nanowells compared to bilayer formation on silica nanowells **(D)** Summary of ζ values with error margins. For niobia nanowells, NeutrAvidin is used as the reference and for silica nanowells the preceding bilayer is used (Figure and caption from **Paper IV**).

To identify preferential binding, we have analyzed the ζ value before saturation (before the whole surface is covered by proteins), for both silica and niobia nanowells. For niobia nanowells, the ζ was 0.61 ± 0.09 for ten experiments, when the peak shift had reached 0.2 nm (**Figure 25B** and **25D**), which is less than half of the saturation signal (in this case the saturation signal corresponds to peak shift of 0.5 nm). The ζ value of 0.61 ± 0.09 is significantly higher than the reference value

which is 0.40 for NeutrAvidin binding. However, for silica nanowells, the ζ value was not very high compared to experimental uncertainty and it was essential to look at data early in the binding process where we have low protein coverage. Overall, the spectral analysis, which is based on a large number of experiments for both structures, demonstrates that IRSP53 has a tendency to bind to negative membrane curvature compared to a planar surface (**Figure 25**).

There is an inclination in the walls of nanowells when going from the aperture to the bottom of the wells which makes nanowells to have a range of curvatures along their vertical axis (**Paper I**). IRSP53 should prefer ~ 0.05 nm^{-1} which is within the expected curvature range inside the nanowells as the top diameter of nanowells is ~ 80 nm [102]. If one could prepare deep nanowells with perfectly vertical walls and the right diameter, the influence from negative curvature on binding would become even more pronounced. Besides the limitations, we believe that our plasmonic nanowells are a valuable label-free platform for location-specific detection with spectral signature for binding at negative curvature in a qualitative manner.

6.2 Plasmonic Nanostructured Sensor Arrays Reveal Curvature-Dependent Biomolecular Interactions

Plasmonic nanowells together with plasmonic nanodisk array were utilized to probe the influence of nanoscale curvature on membrane-peptide interactions (**Paper III**). Nanowells and nanodisks with different architectural geometry are coated with supported lipid bilayers, thereby providing a surface-templated supported lipid membranes to systematically investigate how membrane curvature influences biomolecular interaction processes. We have utilized an amphipathic α-helical (AH) peptide as a curvature-sensitive probe to investigate the influence of membrane curvature on membrane-peptide interactions [107, 108]. AH peptide is believed to create pores in small lipid vesicles with high positive membrane curvature [107]. The membrane disruption occurs above a certain density of pores in the membrane, induced by AH peptides. This mechanism can be translated into development of antiviral strategies against enveloped viruses [109, 110]. Such possibilities highlight the importance of studying the membrane curvature effects on biomolecular interaction processes. The current approaches to study membrane curvature-dependent effects, however, is limited to studying positive membrane curvature with intact vesicles [109-111].

Preparing surface-templated supported lipid membranes with different types of curvature, including negative curvature, using plasmonic nanostructured sensor arrays would be a promising approach to overcome these challenges.

Nanoplasmonic sensors with different architectural geometries were coated by a conformal layer of supported lipid bilayer (SLB) in order to prepare different types of membrane curvature along the sensor arrays. Plasmonic nanodisks with mainly planar geometry and sharp positive curvature (at the rim of the disks) and also plasmonic nanowells with negatively curved regions (interior of the wells) and planar geometry on the top surface and sharp positive curvature at the rim of the wells provide means to investigate the influence of membrane curvature on membrane-peptide interactions.

Nanowells with diameter of 100 nm (in the gold film) and depth of 200 nm were prepared by short-range ordered colloidal self-assembly in silica (SiO_2), as described in chapter 4. They were then coated by a 20 nm thick silicon nitride layer using PECVD. Despite of the silicon nitride deposition, the conformal coating is referred to as silica coating due to the oxygen plasma treatment [112]. The plasmonic nanodisk structure consists of the array of a shallow Au protrusions with diameter and height of 100 nm and 20 nm, respectively. An overlayer of 10 nm silica is sputtered on the nanodisk arrays to make a suitable interface for creating a conformal SLBs [12]. Plasmonic nanodisks were fabricated by our collaborators (group of Nam-Joon Cho) and the corresponding fabrication process can be found in **Paper III**. **Figure 26** show a schematic cross-section of nanodisks and nanowells coated by SLBs together with a SEM top view of nanodisks (**Figure 26A**). **Figure 26B** illustrates a cross-section image of nanowells, taken by FIB-SEM.

As discussed previously, the asymmetric resonance features in the plasmonic response of nanowells, not only have distinct optical field enhancements, but are also sensitive to specific regions of the sensor geometry which makes location-specific detection feasible. For both sensing platforms the plasmonic measurements were performed in transmission mode. The excitation of surface plasmons in nanodisk arrays is manifested as a peak around 720 nm in the extinction spectra when measured in buffer (see **Figure 26C**). The extinction spectra of nanowells in buffer exhibits a peak and a dip around 675 nm and 835 nm respectively, shown in **Figure 26D**. The absolute plasmonic peak and dip shifts are normalized to the bulk refractive index sensitivity of different sensor surfaces enabling to directly compare the mass adsorbed across different regions

of the sensors as the field extension is similar for both structures [86, 113]. The bulk refractive index sensitivity of the nanodisk peak and nanowells peak and dip was determined to be around 101 nm/RI unit, 136 and 220 nm/RI unit respectively, shown in **Figure 26E** and **26F**.

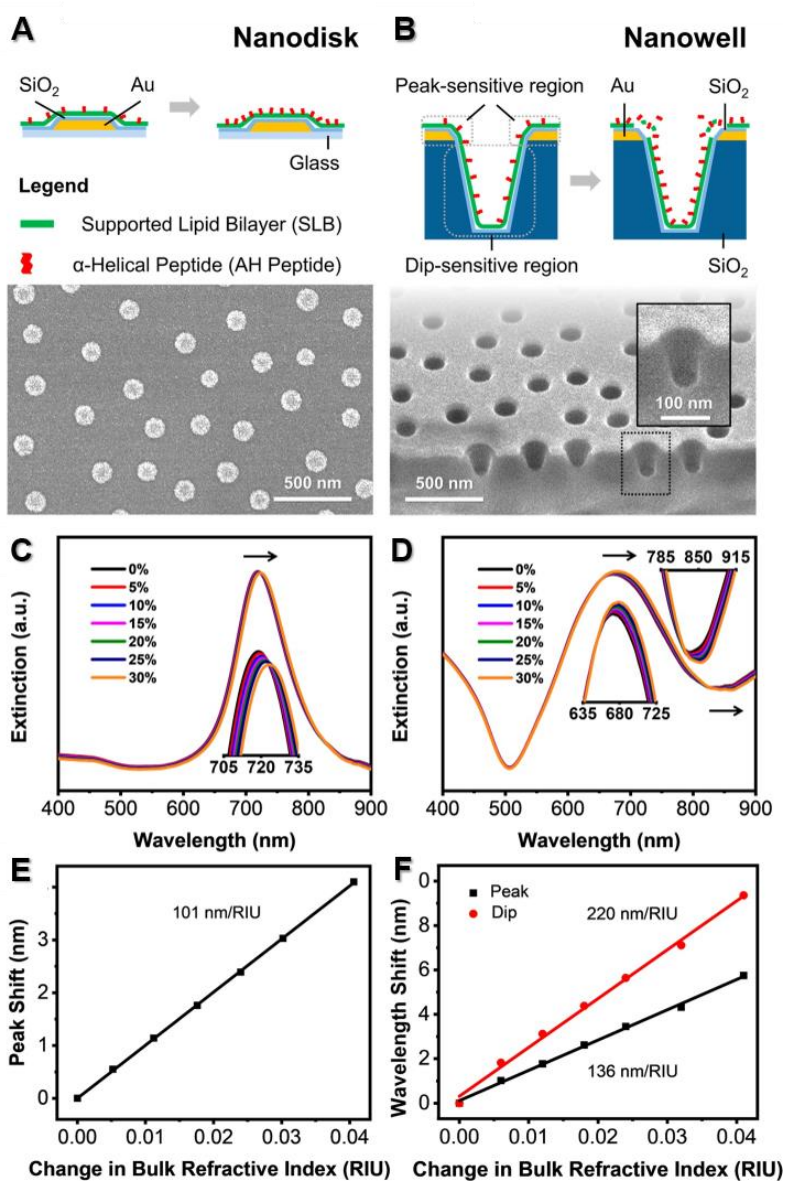

Figure 26. Plasmonic nanodisks and nanowells **(A)** schematic illustration of AH peptide interaction with lipid bilayer-coated nanodisks accompanied by a top view SEM image of plasmonic nanodisks. **(B)** Schematic illustration of AH peptide interaction with SLB-coated nanowells, accompanied by a tilt-angle SEM image of nanowell arrays; the inset shows a closeup of a single nanowell, taken by FIB-SEM. Extinction spectra during buffer-glycerol titration measurements on **(C)** nanodisks **(D)** nanowells. **(E)** Bulk refractive index sensitivity plots of nanodisk peak responses from measurements in (C). **(F)** Bulk refractive index sensitivity plots of nanowells peak and dip responses from measurements in (d) (Figure from **Paper III**).

The SLB formation on silica-coated nanodisks and nanowells using vesicle fusion was confirmed by tracking the plasmonic peak and dip shifts in real time. **Figure 27** represent the resonance shift of the nanostructures upon SLB formation together with the normalized peak and dip sifts to the corresponding bulk refractive index sensitivities. The results indicate that the final peak shift on the nanodisk array was lowest at around 3.0 nm compared to the peak and dip shifts from the nanowells (**Figure 27A**). However, the normalized wavelength shifts of the nanodisk peak, nanowells peak and nanowells dip upon SLB formation were around 0.030, 0.024 and 0.021 RI units respectively (**Figure 27B**). The highest normalized value of peak shift for nanodisks could be due to a slightly more focused electromagnetic field of the nanodisk structure compared to the nanowells, although the field extension of the structures are similar overall [86].

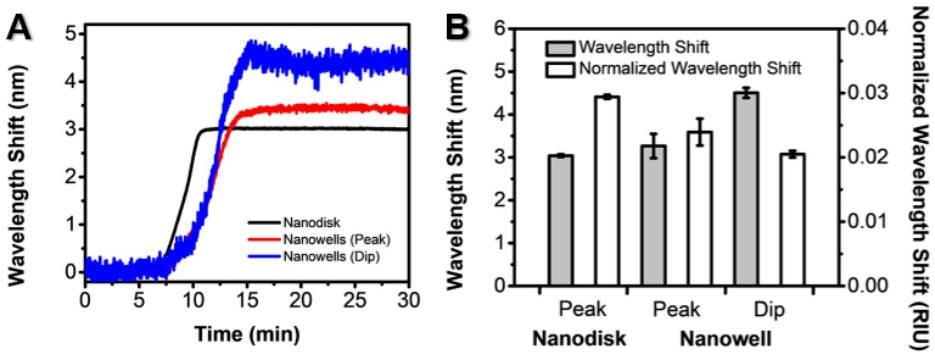

Figure 27. (A) Resonance shift upon SLB formation of silica-coated nanowells and silica-coated nanodisks **(B)** Comparison of final wavelengths shifts upon SLB formation before and after normalization with the respective bulk refractive index sensitivities (Figure form **paper III**).

After establishing a conformal layer of SLB on both nanostructures, we have employed an AH peptide to investigate the influence of curvature on membrane-peptide interactions. The AH peptide was introduced with an increasing concentration to both SLB-coated nanoplasmonic structures while tracking the resonance shifts in real time. **Figure 28A, and 28B** show the resonance shifts and the normalized value of the wavelength shifts to the bulk refractive index sensitivities when increasing the AH peptide concentration from 500 nM to 16 µM. For the SLB-coated nanodisk peak and nanowells dip, a gradual increment in the normalized wavelength shift was observed above the concentration of 2 µM. On the contrary, a gradual decrease in normalized peak shift from the nanowells was observed up to AH peptide concentration of 8 µM, above which a sharp decrease in the normalized peak shift was observed. **Figure 28C** represents that the peak

and dip shift of the nanowells moved in opposite directions above the AH peptide concentration of 2 µM; the peak is blue-shifted while the dip is red-shifted. This indicates striking differences in the membrane-peptide interactions at the nanowells aperture and negatively curved regions of the membrane-coated wells. The peak shift from the nanodisk arrays, mainly arises from the planar regions and the rim (slightly positive curvature) of the nanodisks. Since the nanodisks peak shift showed a similar trend as the nanowells dip shift (both were red-shifted), we can attribute the blue shift from the nanowells peak to highly positive curvature of the upper rim of the wells which is considered as a mainly peak-sensitive region, indicating membrane disruption at the rim of the wells. Of note, the upper rim of the nanowells contains both negative (the interior of the edges) and highly sharp positive curvatures, which makes it challenging to determine which curvature effect dominates in the membrane-peptide interactions. Nevertheless, nanowells extinction dip which is mainly focused on the interior of the wells (negatively curved regions) is not blue shifted. Therefore, the blue-shift in the peak is probably due to the sharp positive curvature of the apertures.

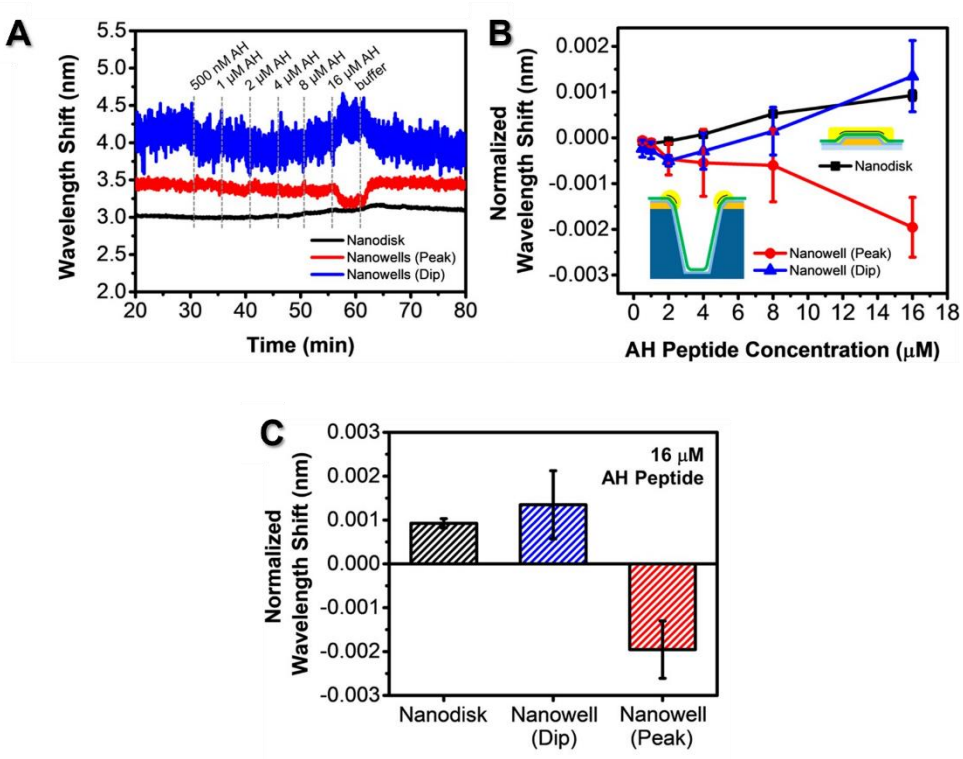

Figure 28. (A) Resonance shift of nanowells and nanodisks upon AH-peptide interaction with SLB-coated nanostructures, with stepwise increase in AH peptide concentration from 500 nM to 16 µM. **(B)** Corresponding plots of normalized peak and the dip wavelength shifts versus AH peptide concentration. **(C)** Comparison of normalized peak and the dip wavelength shifts after the addition of 16 µM AH peptide (Figure from **paper III**).

These observations suggest that the AH peptide binds onto the SLBs with minimal to zero disruption of the membranes at planar and slightly positive curvature regions of the nanodisk and nanowells. However, in the highly positive membrane curvature of the nanowells aperture, the AH peptide adsorbs to the membrane causing concentration-dependent membrane disruption up to a concentration of 8 μM, above which significant membrane disruption occurs, derived from the decrease in the nanowells peak shift. These findings represent another proof for the influence of membrane curvature on the membrane-peptide interactions. Further, we believe that the location-specific detection possibility of our plasmonic nanostructured sensor arrays together with proper spectral analysis, offer a powerful label-free platform for studying curvature-dependent biomolecular interactions.

6.3 Nanoplasmonic Sensing with Functionalized Nanopores in MIM films, Toward a Mimic of the Nuclear Pore Complex

Plasmonic nanopores in suspended metal-insulator-metal films offer a label-free platform for real-time analysis of biomolecular interactions. The unique geometry of nanopores in SiN_x membranes made it possible to functionalize the interior walls of nanopores and therefore, direct protein binding selectively to the interior of the pores. In addition to material-specific sensing, the nanopore geometry was also employed to mimic a nuclear pore complex by immobilizing a certain nucleoporin to the interior walls of the solid state nanopores and detecting a protein transport receptor. This illustrates how nanostructured platforms can be engineered and properly functionalized to study biological nanomachines in a label-free manner. All the materials presented in this section is based on **Paper II**.

Plasmonic nanopores in approximately 50 nm thick SiN_x membranes, coated with double gold films (each film with thickness of 30 nm) were fabricated by colloidal self-assembly and also electron beam lithography, generating short-range ordered and long-range ordered patterns respectively. The nanofabrication processes were described extensively in previous chapters. In the experiments presented in this section, nanopores with two different diameters were fabricated: Nanopores with upper diameter of 170-180 nm and lower diameter of 110-120 nm are referred to as larger pores, while smaller pores exhibit the upper diameter of 80-90 nm in the topside Au film

and lower diameter of 50-60 nm in the bottom side gold film. This variation of ~ 10 nm in diameter is expected when measuring many pores in different positions over the membrane which stems from the size distribution of colloids used for the lithography [60].

Figure 29 shows representative extinction spectra of short-range ordered nanopores with double gold films in water environment. The optical properties and plasmonic response of nanopores were extensively discussed in chapter 5. It is clear from **Figure 29** that reducing diameter of the pores strongly decreases the resonance strength (extinction peak magnitude) and the dip is closer to the peak wavelength. Note that the diameter of smaller pores is at the limit for when the resonance can be identified in the extinction spectrum. Furthermore, the large and small pores were made in different batches with some variation in SiN_x thickness. This influences the coupling between the films and the resonance positions, so the samples should not be compared in this respect.

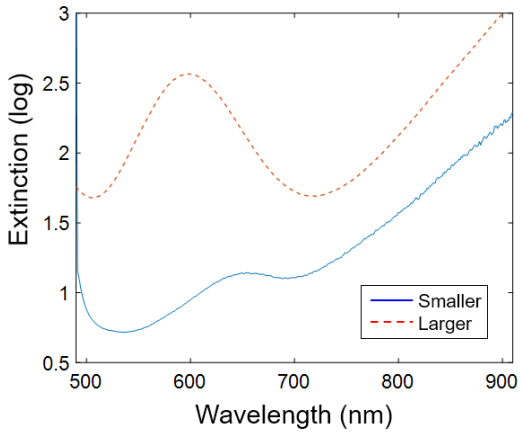

Figure 29. Typical extinction spectra in a water environment for larger (~ 150 nm) and smaller (~ 80) pores, fabricated by short-range ordered colloidal lithography (Figure form **Paper II**).

In order to demonstrate material-specific sensing of nanopores, the interior walls of the nanopores are functionalized such that a model protein binds solely to the interior of nanopores. A schematic view of surface functionalization processes of the nanopores for selective protein binding to the interior of the pores is illustrated in **Figure 30**. The first step in the surface modification is to make the Au films inert toward protein adsorption by binding of relatively short chains of thiolated poly(ethylene glycol) (PEG) to the Au films [10]. This leaves only the silica surface available for the subsequent chemical modification steps [60]. Short chains (2 or 5 kg/mol) of PEG were selected to avoid sealing the pores [13]. Of note, silicon nitride walls are assumed to behave as

silica with respect to chemical modifications due to the presence of a native oxide layer and particularly due to the oxidative cleaning step prior to the experiments.

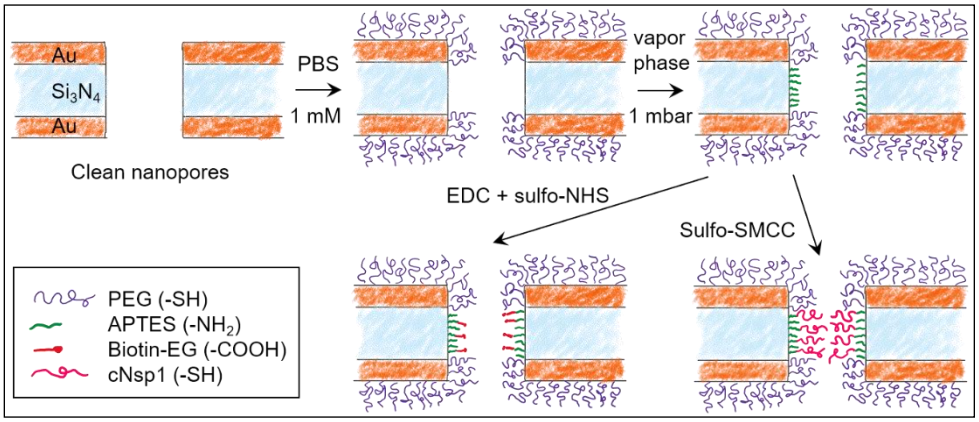

Figure 30. Surface functionalization strategy for immobilizing receptors inside nanopores. After modifying gold with PEG, the nanopore walls are modified with APTES. Receptors can then be bound by cross-linking chemistry between -NH_2 and -COOH (EDC + sulfo-NHS) or between -NH_2 and -SH (sulfo-SMCC). Using sulfo-SMCC is more challenging as it requires that the thiol-PEG coating prevents other thiol groups from reaching the gold (Figure and caption from **Paper II**).

The next step of the chemical modification process was silanization of SiN_x walls (treated as silica surface) using (3-aminopropyl)triethoxysilane (APTES) followed by annealing. The nanopore walls were then functionalized by biotin to investigate the sensor response upon binding of a model protein. Biotin functionalization was achieved by EDC/NHS (1-ethyl-3(3-dimethylaminopropyl)carbodiimide hydrochloride and N-hydroxysulfosuccinimide) conjugation between the amine group on APTES and carboxylic acid groups on the modified biotin. Surface modification protocols for gold and silica surfaces are described in detail in **Paper II**.

We have used conventional SPR and QCM-D to verify surface modification processes on planar gold and silica surfaces. The SPR signal was measured on SPR chips (planar surfaces) before and after deposition of ~ 50 nm SiO_2 using chemical vapor deposition. APTES modification was also verified by SPR indicating a small but clear shift in the reflectivity. The thickness of the APTES was estimated to be 1.5 $\pm$ 0.3 nm with refractive index 1.465 [114], based on the SPR measurements. (**Figure 31A**). Further, binding of a model protein, avidin, to silica sensor crystals was confirmed using QCM-D. **Figure 31B** shows the QCM-D response to avidin binding, followed by binding of biotinylated bovine serum albumin (BSA) to the silica sensors. No

biotinylated BSA binding was observed to the APTES modified silica surfaces in the absence of avidin. This demonstrates that it is truly biotin-avidin binding which results in binding of biotinylated BSA.

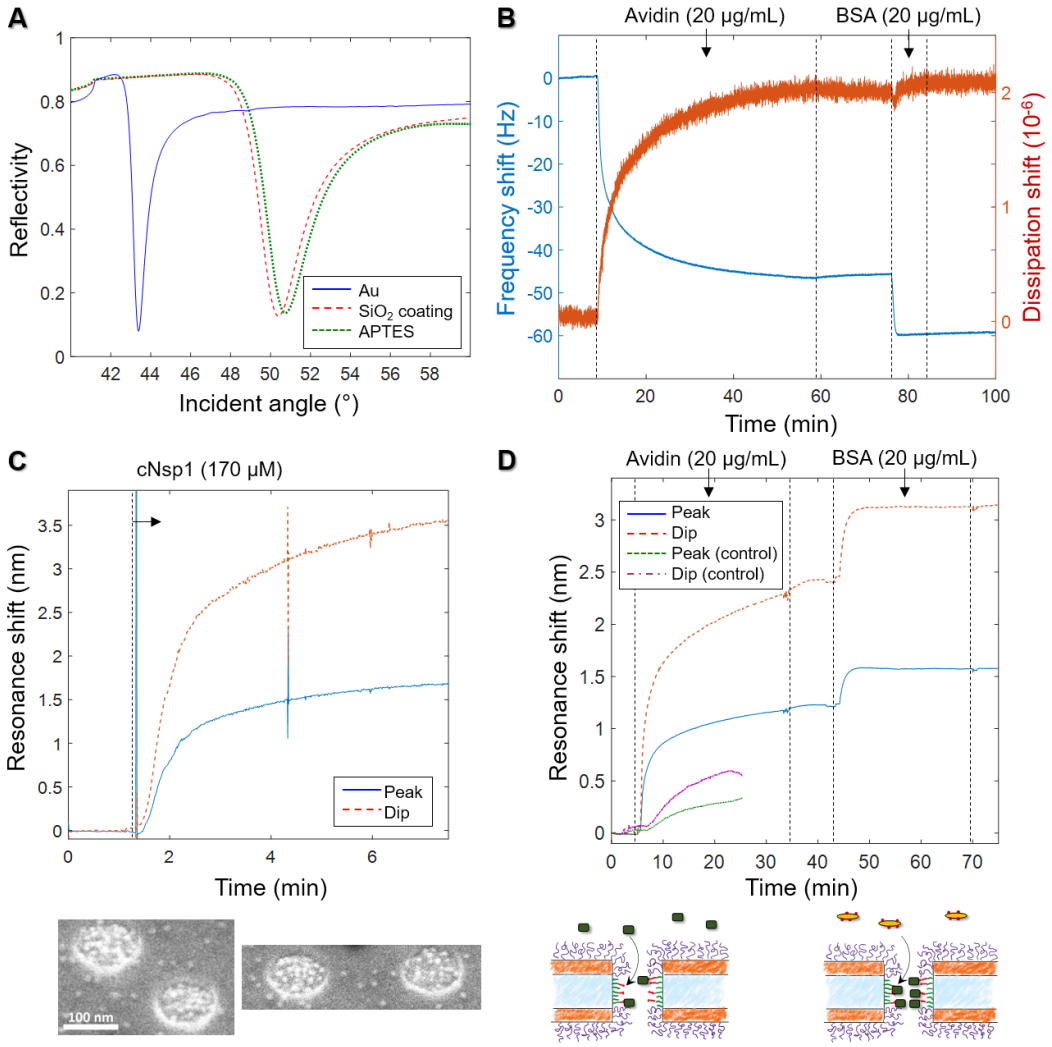

Figure 31. Verification of surface functionalization and model protein binding. **(A)** Angular SPR reflectivity spectra in air (wavelength 670 nm) confirming APTES binding to silica. **(B)** QCMD data showing avidin and subsequent biotin-BSA binding to silica sensor crystal modified with APTES and biotin (as in Figure 30). **(C)** Plasmonic signal from nanopores showing grafting of cNsp1 in PBS buffer to larger pores (after activation by sulfo-SMCC). The images below show enrichment of Kapβ1-modified gold colloids inside pores. **(D)** Detection of avidin and biotin-BSA binding inside larger nanopores, also including a control where no biotinylation was performed on the APTES layer (which gives less and slower binding). The schematics below illustrate the binding events (figure and caption from **Paper II**).

Figure 31D shows the resonance shift upon protein binding to the biotin-modified interior walls of the nanopores by first introducing avidin, followed by biotin-BSA. Each signal corresponds to

binding of a complete monolayer of proteins (avidin or biotin-BSA) since the interaction is irreversible. Much faster biotin-BSA binding was observed compared to avidin binding even though the concentration was similar in both SPR and QCM-D measurements. This can be attributed to a high number of biotin molecules conjugated to the BSA. Assuming BSA as an elongated molecule in solution, BSA can likely interact with several avidin molecules which can consequently cause a faster binding rate [115]. As a control experiment, we have measured resonance shift when avidin was introduced to the nanopores with identically treated walls but without biotinylation step (see **Figure 31D**). Non-specific binding of avidin to the APTES functionalized interior walls was observed but the signal is clearly lower and slower, confirming the presence of biotin molecules inside the pores in other measurements.

In addition to material-specific sensing, our nanoplasmonic sensor offers a unique possibility to mimic a biological nanomachine, the nuclear pore complex (NPC), since the pores are comparable in size and geometry when the diameter of the solid-state nanopores approaches ~ 50 nm [32]. Appropriate surface functionalization of plasmonic nanopores opens up the possibility to mimic the interaction between the transport proteins and the disordered phenylalanine-glycine (FG) nucleoporin domains residing in NPCs [32]. It is also intriguing to investigate how confinement in a solid-state nanopore geometry might influence the binding interactions between the transport receptors and the FG domains compared to the planar SPR surfaces [116, 117].

We have utilized a nuclear import receptor, karyopherinβ1 (Kapβ1) which plays an important role in the transport function and barrier selectivity of the NPC, to investigate interactions with FG domains [117, 118]. FG-rich domains extracted from a yeast nucleoporin Nscp1, referred to as cNsp1, were used to functionalize the interior walls of the solid-state nanopores [30]. The transport receptor, Kapβ1, was added in increasing concentrations to smaller nanopores with cNsp1-modified walls. The resonance shift due to the cNsp1 grafting to larger nanopores in PBS buffer is shown in **Figure 31C.** The inset in **Figure 31C** illustrates the enrichment of Kapβ1-coated gold colloids inside the cNsp1-functionalized nanopores, taken by SEM. **Figure 32A** shows the resonance shift upon Kapβ1 binding to the cNsp1-modified walls in smaller nanopores. It is clear from **Figure 32A** that the peak is barely higher than the noise level and only for the dip wavelength a signal is clearly identified for the smaller nanopores. Still, the data from smaller nanopores is

more interesting since the pore diameter is comparable to the size (inner diameter) of the NPC [31, 32].

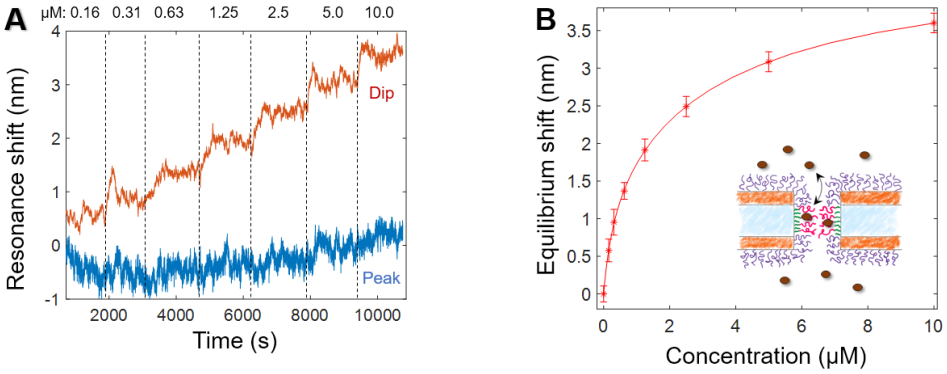

Figure 32. **(A)** Resonance shift upon introducing Kapβ1 in increasing concentrations to smaller nanopores with cNsp1-modified walls. The equilibrium signal is obtained by averaging over time (at least 10 min for each concentration). **(B)** The equilibrium signal vs. Kapβ1 concentration. The curve illustrates a fit to the two component Langmuir model (Figure form **Paper II**).

Figure 32B shows the average dip shift after equilibrium establishment at different concentrations of Kapβ1. These values were fitted to a two component Langmuir isotherm relationship [117]:

$$\Gamma(c) = \Gamma_1 \frac{c}{c + k_1} + \Gamma_2 \frac{c}{c + k_2} \qquad (8)$$

Here the Γ_1 is the maximum surface coverage of species bound in configuration 1 with dissociation constant k_1 and analogously for the Γ_2 and k_2 parameters. The configurations show two different types of binding: the transporters might be either loosely or strongly bound to the immobilized cNsp1, for instance depending on the number of interactions. This modification of the ordinary single binding site Langmuir equilibrium is essential to fit data for transport protein Kapβ1, interacting with immobilized cNsp1 and originates from the multivalency of the interaction that modulates the Kapβ1 binding [116]. We have fitted affinity constants with values of k_1 = 341 nM and k_2 = 3.8 μM, which are very close to the values determined on planar surfaces (k_1 = 0.34 ± 0.06 μM and k_2 = 5.61 ± 1.98 μM) [30]. Our results demonstrate that the negative curvature of the interior walls of the nanopores has no strong influence on the binding affinities. This suggests that the results obtained from the planar surfaces (conventional SPR) can be applicable to the

geometry of the NPCs. However, the main purpose of this work was to demonstrate the possibility of using the geometry of plasmonic nanopores with appropriate surface functionalization to mimic biological nanomachines such as NPCs.

7

Conclusions

In **paper I** I have presented two types of plasmonic nanostructures for label-free real time biomolecular sensing. Fabrication and characterization of two types of plasmonic nanocavities, 'nanowells' and 'nanocaves', together with their sensing properties were described. Short-range ordered colloidal lithography, as a high throughput method, was used to fabricate the solid-supported cavities. The geometry of the nanostructured arrays was characterized by SEM, FIB-SEM and AFM. Plasmonic nanostructures were utilized for location-specific detection of a model protein using appropriate surface functionalization and a proper spectral analysis.

In **paper II**, plasmonic nanopores with double gold films in a ~ 50 nm thick SiN_x membrane was used for label-free detection of protein binding inside the pores. By thiol-based and trietoxysilane chemistry, receptors were selectively positioned on the silicon nitride walls inside the pores. I have used larger nanopores with diameter of ~ 150 nm to detect averaged sized proteins (60 kg/mol) via refractometric sensing. Moreover, we have developed smaller nanopores with diameter of ~ 50 nm which is comparable with the size of nuclear pore complexes. We investigated the transport protein receptor, Kapβ1, binding to the interior walls of the nanopores modified with FG-domain peptides. Comparing the results obtained from nanopores with planar surfaces suggested almost no differences for Kapβ1 binding in the nanopore geometry compared to planar surfaces. This suggests that the results obtained from the planar surfaces can be applicable to the NPC.

In **paper III** nanoplasmonic sensor arrays with different architectural geometries, nanowells and nanodisks, were employed to investigate the influence of membrane curvature on membrane-peptide interactions. The nanostructured arrays coated with conformal supported lipid bilayers, were utilized to study the effect of different curvatures on a curvature-sensitive peptide. Proper

spectral analysis demonstrates a clear difference in membrane-peptide interactions at sensors with different curvatures.

In **Paper IV** we have utilized plasmonic nanowells with two different configurations (cavities in silica and niobia supports) to detect preferential binding of a biologically important protein to lipid membranes with negative curvature compared to planar surfaces. Nanowells were conformally coated with lipid membranes, thereby providing a surface-templated lipid membrane with different curvatures to study the influence of curvature on membrane-protein interactions. The spectral signatures revealed preferential binding to the negatively curved regions of nanowells.

In **Paper V** I have developed long-range ordered arrays of plasmonic nanopores in metal-insulator-metal films in a robust and highly reproducible manner using EBL. Well-ordered arrays of nanopores with double gold films were fabricated in a ~ 50 nm thick SiN_x membrane with either single or double gold films. Short-range ordered arrays of nanopores with the identical structure as EBL pores were also fabricated with two different colloidal lithography approaches. The new colloidal lithography method provides the possibility to create nanopores with a low risk of breaking SiN_x membranes during the lift-off and thereby increases the yield of the fabrication process. EBL offers not only a high control on the arrangement of the nanopores (arbitrary patterns) but also increases the yield of the fabrication process in terms of intact silicon nitride membranes significantly (compared to the old colloidal lithography method, where physical lift-off is performed after the membrane formation). Further, our unique approach, using negative resist during the EBL, prevents the metal from ending up to the pore sidewalls, hence creating metal-free SiN_x walls which can be essential for plasmonic sensing and surface functionalization. We have discussed the influence of aperture ordering for semi-transparent metal films on plasmonic response by creating identical structures (same diameter and surface density) with different aperture ordering. The optical properties were found to be similar with only a few differences between the long-range ordered and short-range ordered arrays of nanopores which were explained by Fano interference between the direct transmission through individual pores in a thin metal film and surface plasmon polaritons in a periodic array.

8

Outlook

7.1 Nanopores for Dielectrophoretic Trapping of Proteins

Plasmonic nanopores in optically thin silicon nitride membranes with double Au films could be a promising label-free platform to trap protein molecules inside the nanopores using dielectrophoresis (DEP), where the two Au films are used as electrodes. The DEP process typically utilizes non-planar electrodes which are subjected to an alternating electric field (AC voltage) to generate an electric field gradient [119]. The nanoobjects inside the electric field are then polarized, resulting in a net force toward or away from the electric field gradient depending on the frequency of the AC voltage and the relative dielectric permittivity of the nanoparticle and surrounding medium [120].

It has been demonstrated that there is a significant increase in adsorption of bovine serum albumin molecules to plasmonic nanohole arrays using DEP, where the electric field gradient was generated between the Au film containing the nanoholes and an indium tin oxide (ITO)-coated glass electrode [26]. Based on simulations, there is a high electric filed gradient at the rim of the nanopores that we have developed, shown in **Figure 33**. The highest magnitude of the electric field is expected to be in the middle of nanopores interior (**Figure 33B**), where the proteins are expected to be captured and remained there due to the electric field gradient.

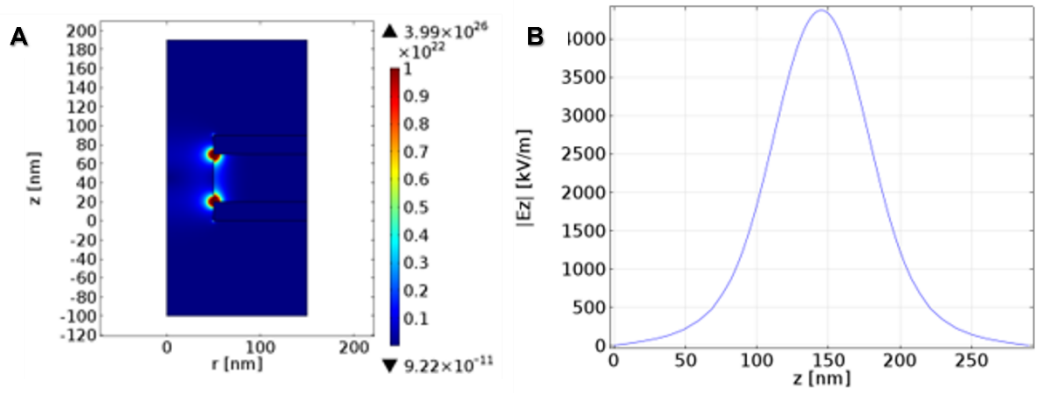

Figure 33. (A) Simulation of electric field gradient across plasmonic nanopores with double gold films using COMSOL **(B)** Simulation of magnitude of the electric field inside the nanopores.

A shift in plasmonic resonance wavelength is expected if proteins are trapped inside the nanopores. Hence, real-time monitoring of the extinction spectra of nanopores can provide information if trapping occurs. For kHz frequencies, the peak and the dip positions in the extinction spectra are not influenced by AC voltage even at high amplitudes of 3V, shown in **Figure 34**, indicating the possibility of performing DEP above kHz and characterizing the DEP trapping by tracking plasmonic signal. However, currently there is not sufficient electrical insulation between the two Au films to perform DEP trapping inside the nanopores. Despite the electrical connection between the two Au films, it is still interesting to investigate the influence of an applied voltage on nanopores functionalized with charged polymer brushes [121]. Dielectrophoretic trapping and control of protein transport through polyelectrolytes could be relevant for applications such as separation of proteins.

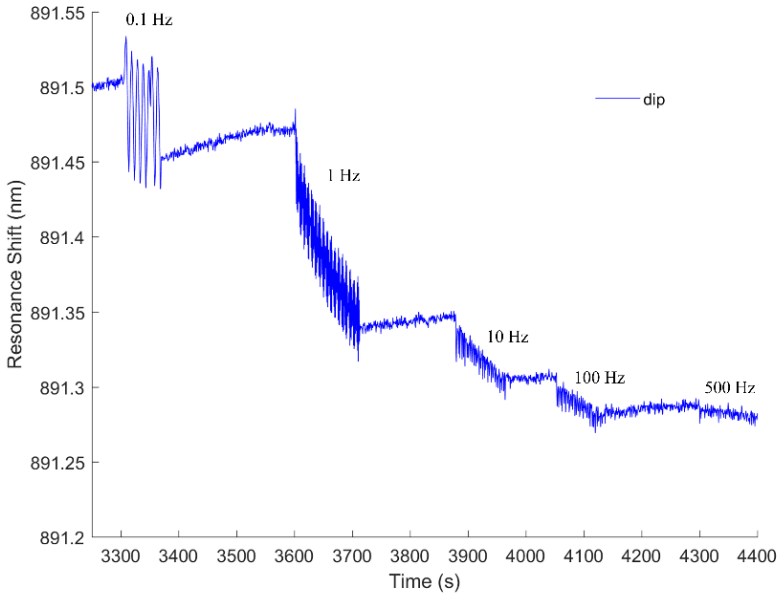

Figure 34. Resonance response (extinction dip) to different frequencies at a certain voltage (300 mV), indicating no resonance shifts above 500 Hz.

7.2 Improving Electrical Insulation in Nanopores

In order to perform DEP trapping (generating electric field gradient inside the pores), it is essential to have an insulating layer between the two gold films across the nanopores. The electrical resistivity of stochiometric silicon nitride (Si_3N_4) thin films, deposited by low-pressure chemical vapor deposition (LPCVD) is expected to be around 10^{15}- 10^{17} Ωcm [122]. Assuming the resistivity of 10^{15}- 10^{17} Ωcm for Si_3N_4 films, electrical resistance in the range of MΩ is expected in our structures (for 50 nm thick Si_3N_4 membrane with the area of ~ 10^4, sandwiched between the two gold films in a 4-inch silicon wafer with thickness of ~ 500 µm). However, I have used low-stress silicon nitride recipe during LPCVD in order to have a high membrane mechanical stability for further fabrication steps, particularly physical lift-off in the CL approach, and also for flow-through experiments. Low-stress silicon nitride recipe results in silicon-rich silicon nitride (SiN_x) films with more conductivity compared to stochiometric silicon nitride (the energy gap reduces from 5 eV to 3-4 eV for Si-rich silicon nitride thin films but still the resistivity of 10^{14} Ωcm is expected) [123, 124]. In our structures, the low-stress recipe resulted in almost no electrical

insulation (a few ohms) through SiN_x membranes with thickness of ~ 50 nm between the two gold films. The electrical resistance measurements were performed using a potentiostat and simply attaching two copper tapes to the Au films at the two sides of the chip/wafer. Among several strategies to find out the source of the electrical contact, and to improve the electrical insulation in the SiN_x membrane sandwiched between double Au films, a few are mentioned below.

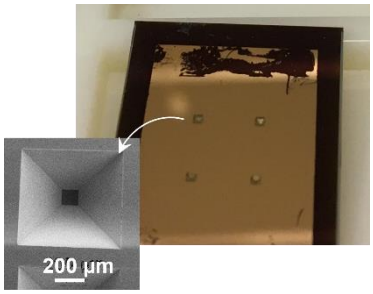

Figure 35. Photo of a chip containing four silicon nitride membranes (backside), coated with Au film. The inset shows a SEM image of the backside of the silicon nitride membrane.

Figure 35 illustrates a photo from the backside of a chip containing (typically four) SiN_x membranes, coated with Au film while carefully protecting the edges of the chip during metal depositions to prevent any electrical contact through the edges. The inset shows a SEM image of a single SiN_x membrane window, imaged from the backside. In order to increase the electrical insulation, an extra layer of SiN_x with thickness of ~ 25 nm was deposited using PECVD on the backside of the chip after creating nanopores in the SiN_x membranes but before deposition of the backside gold film. This resulted in MΩ resistance but with very low reproducibility (only a few chips). Interestingly, even the high-stress silicon nitride recipe during the LPCVD, which is expected to provide stochiometric silicon nitride (Si_3N_4), did not improve the electrical resistance in our structures.

Since Si wafers most probably contribute to the leakage current through the membrane windows, high-resistivity (> 20000 Ωcm) Si wafers were utilized as a supporting substrate for SiN_x membranes, however this resulted in no improvements in the electrical resistance. However, when the stochiometric recipe was combined with high resistivity Si wafers, the resistance was increased up to $10^4\Omega$ at the edge of the wafer (with no nanopores or even SiN_xmembranes), but still a few ohms on chips containing (typically four) SiN_x membranes.

Silicon dioxide (SiO_2) with thickness of ~ 50 nm was thermally grown on the high resistivity Si wafers after forming the SiN_x membranes but before creating nanopores, using thermal oxidation. The intention was to cover the exposed Si surfaces in the 'windows' supporting the membranes. This resulted in the resistance of 10^5 Ω at the edge of the wafers (with no membranes) but only a few ohms at the chips containing the membranes. The next attempt was increasing the thickness of the thermally grown oxide to ~ 400 nm on regular 4-inch Si wafers, in order to see if mega ohm resistance can be achieved. However, the resistance was still $10^5\Omega$.

Approximately 400 nm tetraethyl orthosilicate (TEOS) oxide ($SiO_4C_8H_{20}$), known as a high-quality insulating film, was deposited on regular 3-inch Si wafers (again with no membranes or nanopores) at 710 °C using LPCVD [125]. TEOS oxide deposition resulted in similar resistance ($10^5\Omega$) as thermally grown oxide and mega ohm resistance was not achieved even at the wafers without SiN_x membranes. Assuming 10^5 Ω is sufficient resistance to perform DEP, TEOS oxide coating might improve the insulation across the nanopores up to $10^5\Omega$ even though it requires an extra wet etching (HF) step in the fabrication process of nanopores as TEOS oxide might provide more defect-free films compared to thermally grown oxide.

Acknowledgements

I would like to thank the following people, without whom this thesis would never have been accomplished:

I am most grateful to my supervisor, Professor **Andreas Dahlin**, for giving me the opportunity to experience science. Thank you for your continuous support, enthusiasm for discussions, direct involvement, and all you have taught me. It was a pleasure to work under your supervision.

Dahlin group: I would like to thank former and current members of the Dahlin group, for the nice time we spent together and all your help. It has been a nice group to be a part of.

Martin Andersson: For being a responsible and encouraging examiner.

Marcus Rommel: For co-supervision and the discussions we had. Thanks for teaching me how to make JEOL behave!

Applied Chemistry: For making a nice atmosphere at the division.

My mother, **Maryam**, for all your support, encouragement, and love throughout these years.

Yalda, for being an amazing sister. Thank you for your endless love, support and always being there for me. I am grateful for having the chance to grow up by your side.

My brother-in-law, **Abdolreza**, for all your support and kindness.

My lovely nephew and nieces, **Kasra**, **Syna** and **Ghazal**, for being the best part of my free time, even from far away.

My best friends, **Najmeh** and **Sahar**, for the great time we spent together since the first day of our bachelor's program! Thank you for being there anytime I needed you. Thanks for the unforgettable memories we have and many more to come.

My father, **Mohammad**, for your endless love and always hearing me. I wish I could have had you by my side for more years.

I would like to thank my friends, Maryam, Siamak, Kamran & Parisa, Mehrzad & Farzaneh, Sara, Taha, Pegah, Amin & Elena, Anahid & Pooya, Mohammad Hossein, Samar & Ramin, Alireza, Mona and Maryam & Ali, for the great time we spent together and all your support.

I would also like to thank Knut & Alice Wallenberg Foundation for funding my doctoral studies.

Bita Malekian

Chalmers University

Gothenburg, July 2021

References

1. Zhang, S., et al., *Synthesis, assembly, and applications of hybrid nanostructures for biosensing.* Chem Rev, 2017. **117**(20): p. 12942-13038.
2. Lopez, G.A., et al., *Recent advances in nanoplasmonic biosensors: applications and lab-on-a-chip integration.* Nanophotonics, 2017. **6**(1): p. 123-136.
3. Nelson, P., *Biological physics*. 2004: WH Freeman New York.
4. Dahlin, A.B., *Plasmonic biosensors: an integrated view of refractometric detection.* 2012.
5. Soler, M., et al., *Label-free nanoplasmonic sensing of tumor-associate autoantibodies for early diagnosis of colorectal cancer.* Anal Chim Acta, 2016. **930**: p. 31-38.
6. Jackman, J.A., A.R. Ferhan, and N.-J.J.C.S.R. Cho, *Nanoplasmonic sensors for biointerfacial science.* Chem Soc Rev, 2017. **46**(12): p. 3615-3660.
7. Homola, J.J.C.r., *Surface plasmon resonance sensors for detection of chemical and biological species.* Chem Rev, 2008. **108**(2): p. 462-493.
8. Dahlin, A.B., *Sensing applications based on plasmonic nanopores: The hole story.* Analyst, 2015. **140**(14): p. 4748-4759.
9. Tokel, O., F. Inci, and U.J.C.r. Demirci, *Advances in plasmonic technologies for point of care applications.* Chem Rev, 2014. **114**(11): p. 5728-5752.
10. Emilsson, G., et al., *Strongly stretched protein resistant poly (ethylene glycol) brushes prepared by grafting-to.* Acs Applied Materials & Interfaces, 2015. **7**(14): p. 7505-7515.
11. Oliverio, M., et al., *Chemical functionalization of plasmonic surface biosensors: a tutorial review on issues, strategies, and costs.* ACS Appl Mater Interfaces, 2017. **9**(35): p. 29394-29411.
12. Junesch, J., et al., *Location-specific nanoplasmonic sensing of biomolecular binding to lipid membranes with negative curvature.* Nanoscale, 2015. **7**(37): p. 15080-15085.
13. Emilsson, G., et al., *Polymer brushes in solid-state nanopores form an impenetrable entropic barrier for proteins.* Nanoscale, 2018. **10**(10): p. 4663-4669.
14. Beuwer, M.A., M.W.J. Prins, and P. Zijlstra, *Stochastic Protein Interactions Monitored by Hundreds of Single-Molecule Plasmonic Biosensors.* Nano Letters, 2015. **15**(5): p. 3507-3511.
15. Rosman, C., et al., *Multiplexed plasmon sensor for rapid label-free analyte detection.* Nano Lett, 2013. **13**(7): p. 3243-3247.
16. Brolo, A.G., et al., *Surface plasmon sensor based on the enhanced light transmission through arrays of nanoholes in gold films.* Langmuir, 2004. **20**(12): p. 4813-4815.
17. Dahlin, A., et al., *Localized surface plasmon resonance sensing of lipid-membrane-mediated biorecognition events.* Journal of the American Chemical Society, 2005. **127**(14): p. 5043-5048.
18. Brolo, A.G., et al., *Nanohole-enhanced Raman scattering.* Nano Letters, 2004. **4**(10): p. 2015-2018.
19. Halas, N.J., et al., *Plasmons in strongly coupled metallic nanostructures.* Chemical reviews, 2011. **111**(6): p. 3913-3961.
20. Kumar, S., et al., *Millimeter-sized suspended plasmonic nanohole arrays for surface-tension-driven flow-through SERS.* Chemistry of Materials, 2014. **26**(22): p. 6523-6530.

21. Jeong, Y., et al., *Metal enhanced fluorescence (MEF) for biosensors: General approaches and a review of recent developments.* Biosensors and Bioelectronics, 2018. **111**: p. 102-116.
22. Zhang, Q., et al., *Surface plasmon-enhanced fluorescence on Au nanohole array for prostate-specific antigen detection.* International Journal of Nanomedicine, 2017. **12**: p. 2307.
23. Liu, Y., et al., *Biosensing based upon molecular confinement in metallic nanocavity arrays.* Nanotechnology, 2004. **15**(9): p. 1368.
24. Li, J.-F., C.-Y. Li, and R.F. Aroca, *Plasmon-enhanced fluorescence spectroscopy.* Chemical Society Reviews, 2017. **46**(13): p. 3962-3979.
25. Dahlin, A.B., et al., *Electrochemical plasmonic sensors.* Anal Bioanal Chem, 2012. **402**(5): p. 1773-1784.
26. Barik, A., et al., *Dielectrophoresis-Enhanced Plasmonic Sensing with Gold Nanohole Arrays.* Nano Letters, 2014. **14**(4): p. 2006-2012.
27. Virk, M., et al., *A thermal plasmonic sensor platform: resistive heating of nanohole arrays.* Nano Lett, 2014. **14**(6): p. 3544-3549.
28. Verschueren, D.V., W. Yang, and C.J.N. Dekker, *Lithography-based fabrication of nanopore arrays in freestanding SiN and graphene membranes.* 2018. **29**(14): p. 145302.
29. Kim, J., et al., *Nanoscale mechanism of molecular transport through the nuclear pore complex as studied by scanning electrochemical microscopy.* Journal of the American Chemical Society, 2013. **135**(6): p. 2321-2329.
30. Wagner, R.S., et al., *Promiscuous binding of Karyopherinβ1 modulates FG nucleoporin barrier function and expedites NTF2 transport kinetics.* Biophysical Journal, 2015. **108**(4): p. 918-927.
31. Maimon, T., et al., *The human nuclear pore complex as revealed by cryo-electron tomography.* Structure, 2012. **20**(6): p. 998-1006.
32. Jovanovic-Talisman, T. and A. Zilman, *Protein transport by the nuclear pore complex: simple biophysics of a complex biomachine.* Biophysical Journal, 2017. **113**(1): p. 6-14.
33. Wood, R.W.J.P.R., *Anomalous diffraction gratings.* Physical Review, 1935. **48**(12): p. 928.
34. Fano, U.J.J., *The theory of anomalous diffraction gratings and of quasi-stationary waves on metallic surfaces (Sommerfeld's waves).* Journal of the Optical Society of America, 1941. **31**(3): p. 213-222.
35. Kretschmann, E. and H. Raether, *Radiative decay of non radiative surface plasmons excited by light.* Zeitschrift für Naturforschung A, 1968. **23**(12): p. 2135-2136.
36. Otto, A., *Excitation of nonradiative surface plasma waves in silver by the method of frustrated total reflection.* Zeitschrift für Physik A Hadrons and nuclei, 1968. **216**(4): p. 398-410.
37. Maier, S., *PLASMONICS: FUNDAMENTALS AND APPLICATIONS*. 2007.
38. Xu, Y., et al., *Optical refractive index sensors with plasmonic and photonic structures: promising and inconvenient truth.* Advanced Optical Materials, 2019. **7**(9): p. 1801433.
39. Helmerhorst, E., et al., *Real-time and label-free bio-sensing of molecular interactions by surface plasmon resonance: a laboratory medicine perspective.* Clin Biochem Rev, 2012. **33**(4): p. 161.
40. Homola, J. and M. Piliarik, *Surface plasmon resonance (SPR) sensors*, in *Surface plasmon resonance based sensors*. 2006, Springer. p. 45-67.

41. Curry, A., et al., *Analysis of total uncertainty in spectral peak measurements for plasmonic nanoparticle-based biosensors.* Applied optics, 2007. **46**(10): p. 1931-1939.
42. Haes, A.J. and R.P. Van Duyne, *A nanoscale optical biosensor: sensitivity and selectivity of an approach based on the localized surface plasmon resonance spectroscopy of triangular silver nanoparticles.* Journal of the American Chemical Society, 2002. **124**(35): p. 10596-10604.
43. Ferreira, J., et al., *Attomolar protein detection using in-hole surface plasmon resonance.* Journal of the American Chemical Society, 2009. **131**(2): p. 436-437.
44. Dahlin, A.B., et al., *High-resolution microspectroscopy of plasmonic nanostructures for miniaturized biosensing.* Analytical chemistry, 2009. **81**(16): p. 6572-6580.
45. Dahlin, A., *Biochemical Sensing with Nanoplasmonic Architectures: We Know How but Do We Know Why?* Annual Review of Analytical Chemistry, 2021. **14**.
46. Dekker, C., *Solid-state nanopores.* Nature nanotechnology, 2007. **2**(4): p. 209-215.
47. Lepoitevin, M., et al., *Functionalization of single solid state nanopores to mimic biological ion channels: A review.* Advances in Colloid and Interface Science, 2017. **250**: p. 195-213.
48. Verschueren, D.V., et al., *Label-free optical detection of DNA translocations through plasmonic nanopores.* Acs Nano, 2018. **13**(1): p. 61-70.
49. Lee, K., et al., *Recent Progress in Solid-State Nanopores.* Advanced materials, 2018. **30**(42): p. 1704680.
50. Healy, K., B. Schiedt, and A.P. Morrison, *Solid-state nanopore technologies for nanopore-based DNA analysis.* Nanomedicine (Lond), 2007. **2**(6): p. 875-97.
51. Striemer, C.C., et al., *Charge-and size-based separation of macromolecules using ultrathin silicon membranes.* Nature, 2007. **445**(7129): p. 749-753.
52. Kohli, P., et al., *DNA-functionalized nanotube membranes with single-base mismatch selectivity.* Science, 2004. **305**(5686): p. 984-986.
53. Lee, S.B., et al., *Antibody-based bio-nanotube membranes for enantiomeric drug separations.* Science, 2002. **296**(5576): p. 2198-2200.
54. Spitzberg, J.D., et al., *Plasmonic-Nanopore Biosensors for Superior Single-Molecule Detection.* Advanced materials, 2019. **31**(23): p. 1900422.
55. Valsecchi, C., L.E. Gomez Armas, and J. Weber de Menezes, *Large area nanohole arrays for sensing fabricated by interference lithography.* Sensors, 2019. **19**(9): p. 2182.
56. Verschueren, D.V., W. Yang, and C. Dekker, *Lithography-based fabrication of nanopore arrays in freestanding SiN and graphene membranes.* Nanotechnology, 2018. **29**(14): p. 145302.
57. Zambrana-Puyalto, X., et al., *Site-selective functionalization of plasmonic nanopores for enhanced fluorescence emission rate and Förster resonance energy transfer.* Nanoscale Advances, 2019. **1**(6): p. 2454-2461.
58. Chen, Q., et al., *Fabrication of polygonal nanoholes by localized mask-free wet anisotropic etching.* AIP Advances, 2017. **7**(10): p. 105115.
59. Virk, M., et al., *A thermal plasmonic sensor platform: resistive heating of nanohole arrays.* Nano Letters, 2014. **14**(6): p. 3544-3549.
60. Xiong, K., G. Emilsson, and A.B. Dahlin, *Biosensing using plasmonic nanohole arrays with small, homogenous and tunable aperture diameters.* Analyst, 2016. **141**(12): p. 3803-3810.

61. Cesaria, M., et al., *Gold nanoholes fabricated by colloidal lithography: novel insights into nanofabrication, short-range correlation and optical properties.* Nanoscale, 2019. **11**(17): p. 8416-8432.
62. Cesaria, M., et al., *Long-and Short-Range Ordered Gold Nanoholes as Large-Area Optical Transducers in Sensing Applications.* Chemosensors, 2019. **7**(1): p. 13.
63. Ohno, T., et al., *Hole-size tuning and sensing performance of hexagonal plasmonic nanohole arrays.* Optical Materials Express, 2016. **6**(5): p. 1594-1603.
64. Przybilla, F., C. Genet, and T.W. Ebbesen, *Long vs. short-range orders in random subwavelength hole arrays.* Optics Express, 2012. **20**(4): p. 4697-4709.
65. Dahlin, A.B., et al., *Plasmonic Nanopores in Metal-Insulator-Metal Films.* Advanced Optical Materials, 2014. **2**(6): p. 556-564.
66. Piciu, O., et al., *Fabrication and optical characterization of nano-hole arrays in gold and gold/palladium films on glass.* Proceedings of the Institution of Mechanical Engineers, Part N: Journal of Nanoengineering and Nanosystems, 2007. **221**(3): p. 107-114.
67. Hanarp, P., et al., *Control of nanoparticle film structure for colloidal lithography.* Colloids and Surfaces A: Physicochemical and Engineering Aspects, 2003. **214**(1-3): p. 23-36.
68. Adamczyk, Z. and P. Warszyński, *Role of electrostatic interactions in particle adsorption.* Advances in Colloid and Interface Science, 1996. **63**: p. 41-149.
69. Prikulis, J., et al., *Optical spectroscopy of nanometric holes in thin gold films.* Nano Letters, 2004. **4**(6): p. 1003-1007.
70. Schwind, M., et al., *Diffraction from arrays of plasmonic nanoparticles with short-range lateral order.* Acs Nano, 2012. **6**(11): p. 9455-9465.
71. Oberholzer, M.R., et al., *2-D and 3-D interactions in random sequential adsorption of charged particles.* Journal of colloid and interface science, 1997. **194**(1): p. 138-153.
72. Burmeister, F., et al., *Colloid monolayers as versatile lithographic masks.* Langmuir, 1997. **13**(11): p. 2983-2987.
73. Jansen, H., et al., *A survey on the reactive ion etching of silicon in microtechnology.* Journal of Micromechanics and Microengineering, 1996. **6**(1): p. 14-28.
74. Nguyen, N.-T., *Micromixers: fundamentals, design and fabrication*. Second edition ed. 2012.
75. Yih, P.H., V. Saxena, and A.J. Steckl, *A review of SiC reactive ion etching in fluorinated plasmas.* Physica Status Solidi B-Basic Research, 1997. **202**(1): p. 605-642.
76. Manfrinato, V.R., et al., *Resolution Limits of Electron-Beam Lithography toward the Atomic Scale.* Nano Letters, 2013. **13**(4): p. 1555-1558.
77. Tseng, A.A., et al., *Electron beam lithography in nanoscale fabrication: recent development.* Ieee Transactions on Electronics Packaging Manufacturing, 2003. **26**(2): p. 141-149.
78. Mattox, D.M., *Handbook of physical vapor deposition (PVD) processing*. 2010: William Andrew.
79. Singh, J. and D.E. Wolfe, *Review Nano and macro-structured component fabrication by electron beam-physical vapor deposition (EB-PVD).* Journal of materials Science, 2005. **40**(1): p. 1-26.
80. Sannomiya, T., et al., *Investigation of plasmon resonances in metal films with nanohole arrays for biosensing applications.* Small, 2011. **7**(12): p. 1653-1663.

81. Junesch, J. and T. Sannomiya, *Ultrathin suspended nanopores with surface plasmon resonance fabricated by combined colloidal lithography and film transfer.* Acs Applied Materials & Interfaces, 2014. **6**(9): p. 6322-6331.
82. Zwickl, B., et al., *High quality mechanical and optical properties of commercial silicon nitride membranes.* Applied Physics Letters, 2008. **92**(10): p. 103125.
83. Ring, E., et al., *Silicon nitride windows for electron microscopy of whole cells.* Journal of microscopy, 2011. **243**(3): p. 273-283.
84. Junesch, J., T. Sannomiya, and A.B. Dahlin, *Optical Properties of Nanohole Arrays in Metal-Dielectric Double Films Prepared by Mask-on-Metal Colloidal Lithography.* Acs Nano, 2012. **6**(11): p. 10405-10415.
85. Williams, K.R., K. Gupta, and M. Wasilik, *Etch rates for micromachining processing - Part II.* Journal of Microelectromechanical Systems, 2003. **12**(6): p. 761-778.
86. Mazzotta, F., et al., *Influence of the evanescent field decay length on the sensitivity of plasmonic nanodisks and nanoholes.* Acs Photonics, 2015. **2**(2): p. 256-262.
87. Pacifici, D., et al., *Universal optical transmission features in periodic and quasiperiodic hole arrays.* Optics Express, 2008. **16**(12): p. 9222-9238.
88. Lee, S.H., et al., *Self-assembled plasmonic nanohole arrays.* Langmuir, 2009. **25**(23): p. 13685-13693.
89. Vu Thi, D., et al., *Field localization of hexagonal and short-range ordered plasmonic nanoholes investigated by cathodoluminescence.* The Journal of chemical physics, 2020. **152**(7): p. 074707.
90. Ebbesen, T.W., et al., *Extraordinary optical transmission through sub-wavelength hole arrays.* Nature, 1998. **391**(6668): p. 667-669.
91. Schwind, M., B. Kasemo, and I. Zoric, *Localized and propagating plasmons in metal films with nanoholes.* Nano Letters, 2013. **13**(4): p. 1743-1750.
92. Junesch, J. and T. Sannomiya, *Reflection phase and amplitude determination of short-range ordered plasmonic nanohole arrays.* The journal of physical chemistry letters, 2014. **5**(1): p. 247-252.
93. Rindzevicius, T., et al., *Nanohole plasmons in optically thin gold films.* The Journal of Physical Chemistry C, 2007. **111**(3): p. 1207-1212.
94. Park, T.-H., et al., *Optical properties of a nanosized hole in a thin metallic film.* Acs Nano, 2008. **2**(1): p. 25-32.
95. Gupta, S., *Single-order transmission diffraction gratings based on dispersion engineered all-dielectric metasurfaces.* JOSA A, 2016. **33**(8): p. 1641-1647.
96. Lei, D.Y., et al., *Geometry dependence of surface plasmon polariton lifetimes in nanohole arrays.* Acs Nano, 2010. **4**(1): p. 432-438.
97. Zhang, S., et al., *Heterogeneous forward and backward scattering modulation by polymer-infused plasmonic nanohole arrays.* Journal of Materials Chemistry C, 2019. **7**(10): p. 3090-3099.
98. Kang, E.S., H. Ekinge, and M.P. Jonsson, *Plasmonic fanoholes: on the gradual transition from suppressed to enhanced optical transmission through nanohole arrays in metal films of increasing film thickness.* Optical Materials Express, 2019. **9**(3): p. 1404-1415.
99. Zeno, W.F., et al., *Molecular mechanisms of membrane curvature sensing by a disordered protein.* Journal of the American Chemical Society, 2019. **141**(26): p. 10361-10371.

100. Iversen, L., et al., *Membrane curvature bends the laws of physics and chemistry.* Nature Chemical Biology, 2015. **11**(11): p. 822-825.
101. Jarsch, I.K., F. Daste, and J.L. Gallop, *Membrane curvature in cell biology: An integration of molecular mechanisms.* Journal of Cell Biology, 2016. **214**(4): p. 375-387.
102. Prévost, C., et al., *IRSp53 senses negative membrane curvature and phase separates along membrane tubules.* Nature Communications, 2015. **6**(1): p. 1-11.
103. Mattila, P.K., et al., *Missing-in-metastasis and IRSp53 deform PI (4, 5) P2-rich membranes by an inverse BAR domain–like mechanism.* The Journal of cell biology, 2007. **176**(7): p. 953-964.
104. Saarikangas, J., et al., *Molecular mechanisms of membrane deformation by I-BAR domain proteins.* Current biology, 2009. **19**(2): p. 95-107.
105. Jonsson, M.P., et al., *Supported lipid bilayer formation and lipid-membrane-mediated biorecognition reactions studied with a new nanoplasmonic sensor template.* Nano Letters, 2007. **7**(11): p. 3462-3468.
106. Jonsson, M.P., P. Jönsson, and F. Höök, *Simultaneous nanoplasmonic and quartz crystal microbalance sensing: Analysis of biomolecular conformational changes and quantification of the bound molecular mass.* Analytical chemistry, 2008. **80**(21): p. 7988-7995.
107. Jackman, J.A., et al., *Rupture of lipid vesicles by a broad-spectrum antiviral peptide: influence of vesicle size.* The Journal of Physical Chemistry B, 2013. **117**(50): p. 16117-16128.
108. Hatzakis, N.S., et al., *How curved membranes recruit amphipathic helices and protein anchoring motifs.* Nature Chemical Biology, 2009. **5**(11): p. 835-841.
109. Jackman, J.A., et al., *Correlation between membrane partitioning and functional activity in a single lipid vesicle assay establishes design guidelines for antiviral peptides.* Small, 2015. **11**(20): p. 2372-2379.
110. Tabaei, S.R., et al., *Single vesicle analysis reveals nanoscale membrane curvature selective pore formation in lipid membranes by an antiviral α-helical peptide.* Nano Letters, 2012. **12**(11): p. 5719-5725.
111. Jackman, J.A., et al., *Deciphering how pore formation causes strain-induced membrane lysis of lipid vesicles.* Journal of the American Chemical Society, 2016. **138**(4): p. 1406-1413.
112. Jime, C., et al., *Transformation of silicon nitride in oxygen plasma.* Surface and Coatings Technology, 1991. **45**(1-3): p. 147-154.
113. Jackman, J.A., et al., *Nanoplasmonic ruler to measure lipid vesicle deformation.* Chemical Communications, 2016. **52**(1): p. 76-79.
114. Howarter, J.A. and J.P. Youngblood, *Optimization of silica silanization by 3-aminopropyltriethoxysilane.* Langmuir, 2006. **22**(26): p. 11142-11147.
115. Tominaga, R., et al., *Visible detection of biotin by thin-film interference: thickness control through exchange reaction of biotin/dethiobiotin–avidin bonding.* Journal of Materials Chemistry, 2008. **18**(9): p. 976-980.
116. Schoch, R.L., L.E. Kapinos, and R.Y. Lim, *Nuclear transport receptor binding avidity triggers a self-healing collapse transition in FG-nucleoporin molecular brushes.* Proceedings of the National Academy of Sciences, 2012. **109**(42): p. 16911-16916.

117. Kapinos, L.E., et al., *Karyopherin-centric control of nuclear pores based on molecular occupancy and kinetic analysis of multivalent binding with FG nucleoporins.* Biophysical Journal, 2014. **106**(8): p. 1751-1762.
118. Kapinos, L.E., et al., *Karyopherins regulate nuclear pore complex barrier and transport function.* Journal of Cell Biology, 2017. **216**(11): p. 3609-3624.
119. Ertsgaard, C.T., et al., *Integrated nanogap platform for sub-volt dielectrophoretic trapping and real-time Raman imaging of biological nanoparticles.* Nano Letters, 2018. **18**(9): p. 5946-5953.
120. Nakano, A. and A. Ros, *Protein dielectrophoresis: advances, challenges, and applications.* Electrophoresis, 2013. **34**(7): p. 1085-1096.
121. Ferrand-Drake del Castillo, G., G. Emilsson, and A. Dahlin, *Quantitative analysis of thickness and pH actuation of weak polyelectrolyte brushes.* The Journal of Physical Chemistry C, 2018. **122**(48): p. 27516-27527.
122. Joshi, B., et al., *LPCVD and PECVD silicon nitride for microelectronics technology.* Indian Journal of Engineering and Materials Sciences, 2000. **7**(5-6): p. 303-309.
123. Vasileiadis, N., et al., *Understanding the role of defects in silicon nitride-based resistive switching memories through oxygen doping.* IEEE Transactions on Nanotechnology, 2021. **20**: p. 356-364.
124. Tao, M., et al., *Electrical conduction in silicon nitrides deposited by plasma enhanced chemical vapour deposition.* Philosophical Magazine B, 1996. **73**(4): p. 723-736.
125. Tochitani, G., M. Shimozuma, and H. Tagashira, *Deposition of silicon oxide films from TEOS by low frequency plasma chemical vapor deposition.* Journal of Vacuum Science & Technology A: Vacuum, Surfaces, and Films, 1993. **11**(2): p. 400-405.